Int J Fract
https://doi.org/10.1007/s10704-023-00703-0

RESEARCH

Revisiting facet nucleation under mixed mode I+III loading with T-stress and mode-dependent fracture properties

Aurélien Doitrand · Dominique Leguillon · Gergely Molnár · Véronique Lazarus

Received: 16 November 2022 / Accepted: 7 May 2023

Abstract We study the problem of crack front segmentation into facets under mixed mode I+III loading. Discrete facet network nucleation is determined based on the match asymptotic expansion approach of the coupled criterion considering both the influence of T-stress (parallel to the initial crack front) and mode-dependent fracture properties. We show that considering exclusively either T-stress or mode dependent properties, facet nucleation may be more favorable than straight crack propagation but in conditions that are incompatible with experimental observations. It is only by coupling mode-dependent fracture properties with T-stress that we are able to determine configurations compatible with experimental observations for which facet nucleation is more likely to occur than straight crack propagation. These configurations depend on the T-stress magnitude and critical shear energy release rate. We thus highlight that crack front segmentation into facets is material and loading dependent phenomenon that is not related to a sole mode mixity threshold but also to T-stress magnitude and shear critical energy release rate.

Keywords Mode I+III · Crack nucleation · Crack front segmentation · T-stress

A. Doitrand (✉)
Univ Lyon, INSA-Lyon, UCBL, CNRS, MATEIS, UMR5510, 69621 Villeurbanne, France
e-mail: aurelien.doitrand@insa-lyon.fr

D. Leguillon
Institut Jean Le Rond d'Alembert, Sorbonne Université, CNRS UMR 7190, Paris, France

G. Molnár
Univ Lyon, CNRS, INSA-Lyon, LaMCoS, UMR5259, 69621 Villeurbanne, France

V. Lazarus
IMSIA, ENSTA Paris, CNRS, EDF, CEA, Institut Polytechnique de Paris, 828 boulevard des Maréchaux, 91762 Palaiseau cedex, France

1 Introduction

In the context of linear elastic fracture mechanics (LEFM), the propagation of a crack loaded in mode I+II is nowadays generally well predicted (Erdogan and Sih 1963; Pham et al. 2017) using symmetry arguments (Goldstein and Salganik 1974) or Griffith's energy minimization principles (Francfort and Marigo 1998). It is less straightforward when some amount of mode III is present mainly because of the intrinsic three-dimensional character of the problem and the complexity of the propagation path topology. Fracture under mixed mode I+III loading has been studied since the first experimental works of Sommer (1969) who highlighted lance-like fracture facets in Knauss (1970), Palaniswamy and Knauss (1978) who evidenced the formation of penny-shaped fracture surfaces straddling the original straight crack front in a crossed linked polymer. The complex fracture pattern induced by such a loading has since then been evidenced in other materials and configurations such as for instance fault forma-

Published online: 20 May 2023

tion (Cox and Scholz 1988; Pollard et al. 1982), cracks in rocks (Younes and Engelder 1999), polymers (Buchholz et al. 2004; Chen et al. 2015; Hull 1994; Lazarus et al. 2008; Lin et al. 2010), metals (Vojtek et al. 2016, 2013), gels (Ronsin et al. 2014) or even cheese (Goldstein and Osipenko 2012).

A commonly used test is 3- or 4-points single edge notched bending performed on rectangular beams containing a crack inclined with respect to mode I (Fig. 1a) (Lazarus et al. 2001; Lin et al. 2010).

In this setup, a rotation of the original straight crack toward a pure mode I propagation configuration is observed at the macroscale, but closer look at the crack surface indicates that it rather has the shape of a saw-tooth factory roof. This particular profile actually originates from the formation of small aligned facets along the initial crack front (Fig. 1b). The macroscopic rotation results from the presence of mode II that changes sign on either side of the front (Lazarus et al. 2008) since the crack opens onto free edges (Dhondt et al. 2001). Hence it is usually well captured by fracture propagation simulations based on LEFM and the Principle Local Symmetry (Goldstein and Salganik 1974) or equivalently Griffith's based energy minimization principle (Amestoy and Leblond 1992), using for instance extended finite element method (Gravouil et al. 2002), virtual crack closure integral method (Buchholz et al. 2004; Dhondt et al. 2001; Lazarus et al. 2008), dual boundary element modeling (Citarella and Buchholz 2008), eigen erosion (Pandolfi and Ortiz 2012) or phase-field approach to fracture (Molnár et al. 2022; Pham and Ravi-Chandar 2017). The facets originate from the presence of a dominant mode III over mode II contribution at the center of the crack front (Lazarus et al. 2008). Some of these facets then grow and finally coalesce (Fig. 1b) due to the shielding interaction between facets (Pham and Ravi-Chandar 2014). In spite of their complexity, this crack topology can be obtained accurately by propagating already existing facets following classical LEFM rules, as has been evidenced by continuum phase field simulations (Chen et al. 2015; Henry 2016; Pham and Ravi-Chandar 2017).

Although generally occurring in presence of mode III, crack front segmentation into facets does not develop systematically (Eberlein et al. 2017; Ronsin et al. 2014). Several authors related the occurrence of facets to a certain threshold in terms of mode III (K_{III}) to mode I (K_I) stress intensity factor (SIF) ratio. For instance, Eberlein et al. (2017) showed experimentally that in some configurations, below $K_{III}/K_I = 0.57$ threshold, no facet formation is observed and the crack grows continuously. Facets observed by Sommer (1969) were obtained for $K_{III}/K_I = 0.06$. Cambonie and Lazarus evidenced the presence of facets for K_{III}/K_I ratios between 0.1 and 0.6. Pham and Ravi-Chandar observed facets for $K_{III}/K_I = 0.58$ (Pham and Ravi-Chandar 2016), but also for a very small $K_{III}/K_I = 0.001$ threshold in another configuration (Pham and Ravi-Chandar 2014). Finally, it seems that there is no clear experimental consensus regarding the existence of a K_{III}/K_I threshold for facet nucleation. At least if this threshold is a condition for the facet appearance, it is obviously not the only one.

Toughening induced by the presence of mode III has been reported in several experiments (Davenport and Smith 1993; Eberlein et al. 2017; Hattali et al. 2021; Lin et al. 2010; Liu et al. 2004). Using a two-scale cohesive zone (CZ) model (Lazarus et al. 2020; Leblond et al. 2015), this increasing resistance to fracture has been shown to be due to the presence of facets at the microscale, whose further propagation requires a higher load than the one promoting a smooth propagation (Hattali et al. 2021). The toughness increase can be determined by the CZ model provided the existence of facets whose geometry can be described by profilometry measurements (Cambonie and Lazarus 2014). Nevertheless, a self-sufficient prediction requires a better understanding of why and how crack front segmentation into facets occurs from the initial crack.

The formation of facets was tackled from two different points of view. The first one considers that facets develop by continuous propagation of all the points of the initial crack following stability and bifurcation arguments. The second one considers that the facet segmentation results from the nucleation of new cracks that are connected to the initial crack front along a discontinuous set of points. In presence of mode III, straight crack propagation may be unstable and the development of a segmented crack front may be favored. It has been evidenced numerically by phase-field simulations (Pons and Karma 2010) and confirmed by a thorough closed-form linear stability analysis of the problem (Leblond et al. 2011). This analysis evidenced the existence of a theoretical threshold K_{III}/K_I depending on the material's Poisson's ratio below which straight propagation is expected to occur. It is however generally too large compared to that measured experimen-

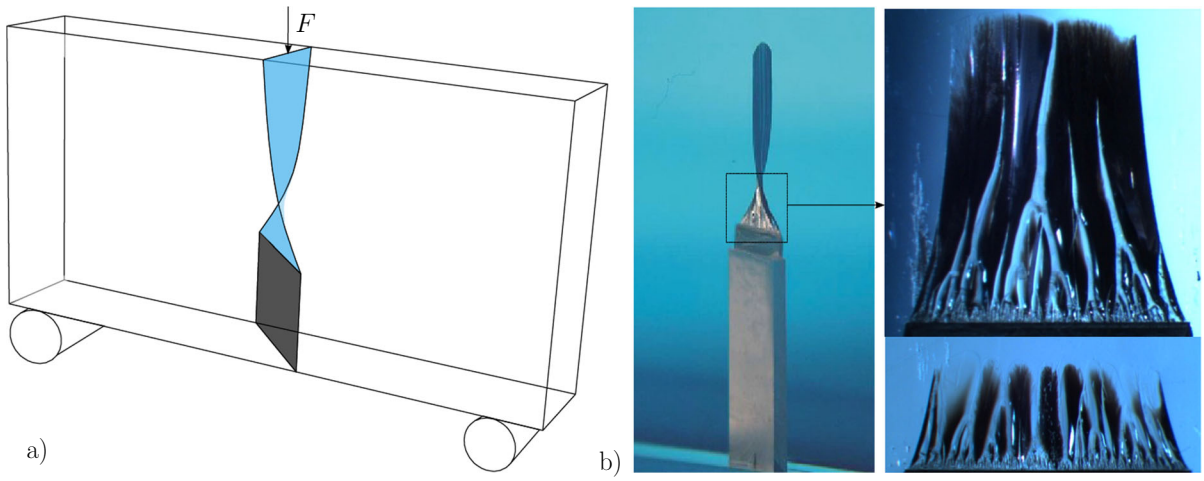

Fig. 1 **a** Macroscale illustration of straight inclined crack rotation towards pure mode I propagation configuration under three point bending. **b** Experimental observation of saw-tooth factory roof crack. The length of the initial crack front before segmentation is about 12 mm

tally (Pham and Ravi-Chandar 2014). The instability has been shown to be subcritical (Chen et al. 2015), meaning that even below the linear stability threshold, out-of-plane propagation may occur in line with experimental observations, if the number of defects is high enough. The number of required defects needed to trigger the instability remains however unknown, and the linear stability threshold may express below this level. Dependance of the fracture energy on the mode mixity ratio has been shown to reduce the threshold (Leblond et al. 2019). However non-physical fracture energy values had to be used to retrieve thresholds measured experimentally. This limitation was recently improved by considering the influence of non-singular stresses (T-stresses) on the stability threshold (Lebihain et al. 2022). It was observed, in some experiments allowing observation at small scales, that the propagation does apparently not occur by propagation of all the point of the crack front but rather by spontaneous nucleation of new cracks from isolated points (Pham and Ravi-Chandar 2016). These facet nucleations may be at the origin of the instability development, in other words they may form the required defects to trigger the subcritical instability. Why and how facets nucleate still remains unclear. Facet nucleation under mixed mode I+III loading was studied numerically by Mittelman and Yosibash (2015), Yosibash and Mittelman (2016) and Doitrand and Leguillon (2018). These works made it possible to predict the initiation loading level of one facet (Yosibash and Mittelman 2016) or of a periodic array of facets (Doitrand and Leguillon 2018) based on the coupled criterion (CC) (Leguillon 2002), assuming that the crack orientation is defined by the direction maximizing the stress normal to the crack plane. The crack shape was either idealized (Mittelman and Yosibash 2015; Yosibash and Mittelman 2016) or defined by stress isocontours (Doitrand and Leguillon 2018), which yielded crack shapes close to the shapes observed experimentally by Pham and Ravi-Chandar (2016). Nevertheless, in these studies, the predicted loading level at facet initiation was actually larger than the one obtained for straight propagation of the initial crack front predicted by LEFM. In our previous work (Doitrand and Leguillon 2018), both non-singular stresses and mode-dependent fracture parameters were disregarded in the analysis. But they may both have an influence on the facet initiation loading level as well as facet geometrical features. The objective of this work is thus to revisit the problem of facet nucleation using the CC by investigating the influence of T-stress as well as of mode-dependent fracture properties. We present the matched asymptotic expansion approach of the CC to predict facet nucleation and its numerical implementation in Sects. 2 and 3, then we study the influence of T-stress and mode-dependent fracture properties on facet nucleation in Sects. 4, 5, and 6.

2 Determination of the incremental energy release rate

2.1 Matched asymptotic approach

We study the problem of sharp rectilinear crack front loaded in combined mode I+III+T-stress. We only focus on the T-stress component T_3 parallel to the crack front direction (Ox_3) (Fig. 2). We consider two possible scenario, namely either crack propagation in the initial crack direction (Fig. 2c) or crack front segmentation into an array of small facets that are inclined with respect to the initial crack direction, as depicted in Fig. 2a.

Experimental observations show that the facet network is almost periodic (Pham and Ravi-Chandar 2016). Therefore, it can be modeled by periodically repeating a representative volume element containing a single facet (Fig. 2d). Straight crack propagation or facet nucleation is assessed based on the matched asymptotic (MA) approach of the CC (Doitrand and Leguillon 2018, 2021; Doitrand et al. 2020a, b; Leguillon 2002). It consists in considering a two-scale 3D problem to solve under linear elasticity and small deformations assumption. The first problem is written at the specimen scale. The displacement field $\boldsymbol{U}^\ell$ (the superscript ℓ refers to the presence of a crack extension ℓ along (Ox_1) direction) is solution of the following set of equations:

$$\begin{cases} -\nabla \cdot \underline{\sigma}(\boldsymbol{U}^\ell) = 0, \\ \underline{\sigma}(\boldsymbol{U}^\ell) = \underline{\underline{C}} : \nabla^s \boldsymbol{U}^\ell, \\ \underline{\sigma}(\boldsymbol{U}^\ell) \cdot \boldsymbol{n} = \boldsymbol{0} \text{ along the crack faces}, \\ \boldsymbol{n} \text{ is the normal to the crack face}, \end{cases} \tag{1}$$

where $\underline{\sigma}$ and $\underline{\underline{C}}$ respectively are the stress and stiffness tensors. It is assumed that the unknown crack extension ℓ at initiation is relatively small compared to the specimen dimensions, this assumption has to be checked afterwards to ensure the validity of the MA approach. Therefore, the actual solution can be approximated by:

$$\boldsymbol{U}^\ell(x_1, x_2, x_3) = \boldsymbol{U}^0(x_1, x_2, x_3) + \text{ small correction}, \tag{2}$$

where $\boldsymbol{U}^0(x_1, x_2, x_3)$ is the solution to a problem without crack extension ($\ell = 0$) and the small correction is actually determined by solving the second problem, close to the crack tip. This approximation is valid except near the initial crack tip, it is called the outer field. The asymptotic displacement field corresponding to an initial sharp crack under mode I+III+T-stress loading can be written as:

$$\begin{aligned} \boldsymbol{U}^0(x_1, x_2, x_3) &= \boldsymbol{U}^0(0, 0, 0) + K_\mathrm{I}\sqrt{r}\boldsymbol{u}_\mathrm{I}(\theta) \\ &+ K_\mathrm{III}\sqrt{r}\boldsymbol{u}_\mathrm{III}(\theta) + T_3 r \boldsymbol{t}(\theta) + ..., \end{aligned} \tag{3}$$

where K_I and K_III are mode I and III stress intensity factors, T_3 is the T-stress magnitude, $\mathbf{u}_\mathrm{I}$, $\mathbf{u}_\mathrm{III}$ and $\mathbf{t}$ are the corresponding angular functions, r and θ are spherical coordinates. For the sake of simplicity, we will omit the dependency to the second angle in spherical coordinates since mode II is not considered in this work. The previous equation can be rewritten:

$$\begin{aligned} \boldsymbol{U}^0(x_1, x_2, x_3) &= \boldsymbol{U}^0(0, 0, 0) + K_\mathrm{I}\sqrt{r}(\boldsymbol{u}_\mathrm{I}(\theta) \\ &+ m\boldsymbol{u}_\mathrm{III}(\theta) + m_T(r)\boldsymbol{t}(\theta) + ...), \end{aligned} \tag{4}$$

where the mode mixities m and m_T are defined so that $m = K_\mathrm{III}/K_\mathrm{I}$, and $m_T(r) = \sqrt{r}T_3/K_\mathrm{I}$. The corresponding expansion of the stress field is obtained using Hooke's law:

$$\begin{aligned} \underline{\sigma}^0(x_1, x_2, x_3) &= \frac{K_\mathrm{I}}{\sqrt{r}}\big(\underline{s}^\mathrm{I}(\theta) + m\underline{s}^\mathrm{III}(\theta) \\ &+ m_T(r)\underline{\tau}(\theta) + ...\big). \end{aligned} \tag{5}$$

To have a detailed form of the actual solution $\boldsymbol{U}^\ell$, the initial domain is rescaled by $1/\ell$. We define the new dimensionless space variables as $y_i = x_i/\ell$. As ℓ tends towards 0, the corresponding domain becomes unbounded. The crack extension along (Ox_1) direction is thus 1 in the dilated domain, which is called the inner domain. The inner domains in the two possible initiation configurations (crack extension in the initial direction of crack front segmentation) are depicted in Fig. 2. The actual solution (with crack extension) is assumed to expand in the following way:

$$\begin{aligned} &\boldsymbol{U}^\ell(x_1, x_2, x_3) \\ &= \boldsymbol{U}^\ell(\ell y_1, \ell y_2, \ell y_3) \qquad = F_0(\ell)\boldsymbol{V}^0(y_1, y_2, y_3) \\ &\quad + F_1(\ell)\boldsymbol{V}^1(y_1, y_2, y_3) \\ &\quad + F_2(\ell)\boldsymbol{V}^2(y_1, y_2, y_3) \\ &\quad + ..., \end{aligned} \tag{6}$$

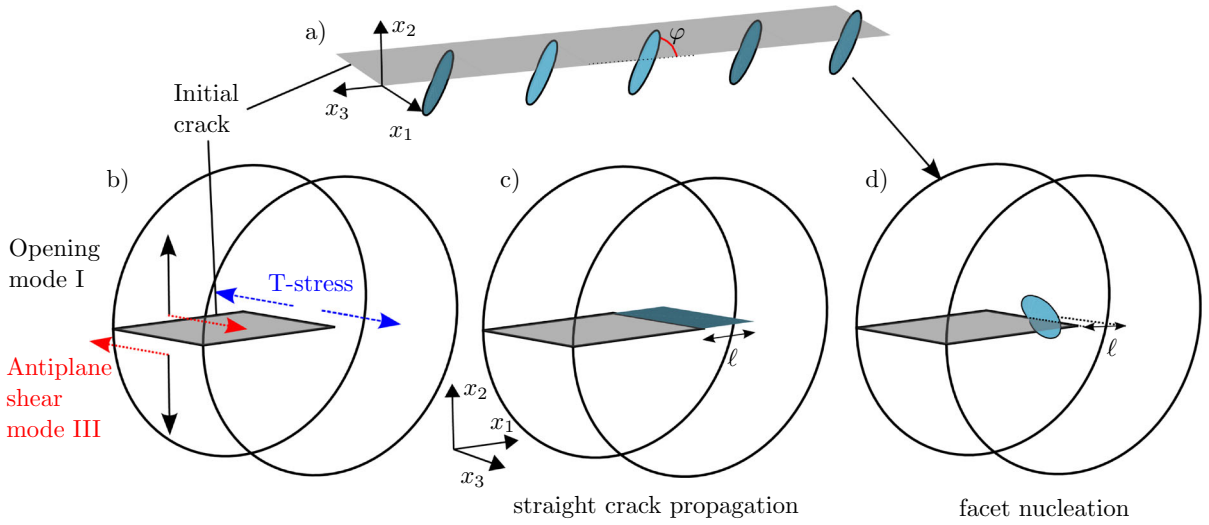

Fig. 2 **a** Illustration of crack front segmentation into a periodic array of inclined facets, **b** illustration of the initial crack front configuration under mode I + III + T-stress and representative volume element of crack propagation configuration, **c** along the initial front direction or **d** by crack front segmentation into a facet network

with

$$\lim_{\ell \to 0} \frac{F_{i+1}(\ell)}{F_i(\ell)} = 0. \tag{7}$$

The $\boldsymbol{V}^i$ form the inner field, they are solutions to problems with prescribed behavior at infinity. They fulfil the usual balance equation, boundary conditions and the linear elastic constitutive law derived from the original problem. They must match at infinity with the behavior of the far field. Therefore, there exists an area, far from the free edge in the inner expansion and close to it in the outer expansion where both expansions given in Eqs. (2) and (6) hold true. Matching the terms in Eqs. (3) and (6) leads to:

$$\begin{cases} F_0(\ell) = 1, \\ \boldsymbol{V}^0(y_1, y_2, y_3) = \boldsymbol{U}^0(0, 0, 0), \\ F_1(\ell) = K_{\mathrm{I}}\sqrt{\ell}, \\ \boldsymbol{V}^1(y_1, y_2, y_3) \approx \sqrt{\rho}(\boldsymbol{u}_I(\theta) + m\boldsymbol{u}_{\mathrm{III}}(\theta)), \\ F_2(\ell) = T_3\ell, \\ \boldsymbol{V}^2(y_1, y_2, y_3) \approx \rho \boldsymbol{t}(\theta), \end{cases} \tag{8}$$

where $\rho = r/\ell$. The symbol $\approx$ means "behaves like at infinity", the $\boldsymbol{V}^i$ can thus be written as:

$$\begin{cases} \boldsymbol{V}^1(y_1, y_2, y_3) = \sqrt{\rho}(\boldsymbol{u}_I(\theta) + m\boldsymbol{u}_{III}(\theta)) \\ \quad + \hat{\boldsymbol{V}}^1(y_1, y_2, y_3), \\ \boldsymbol{V}^2(y_1, y_2, y_3) = \rho \boldsymbol{t}(\theta) + \hat{\boldsymbol{V}}^2(y_1, y_2, y_3). \end{cases} \tag{9}$$

We have to prove the existence of $\hat{\boldsymbol{V}}^i(y_1, y_2, y_3)$ and to verify the equilibrium equations. By combining Eqs. (6) and (8) into Eq. (1), $\hat{\boldsymbol{V}}^i$ is solution to the following problem:

$$\begin{cases} -\nabla_y \cdot \hat{\underline{\sigma}}^i = 0 \text{ where } \nabla_y = \frac{1}{\ell}\nabla_x, \\ \hat{\underline{\sigma}}^i = \underline{\underline{C}} : \nabla_y^s \hat{\boldsymbol{V}}^i, \\ \hat{\underline{\sigma}}^1 \cdot \boldsymbol{n} = -(\frac{1}{\sqrt{\rho}}\underline{s}_I(\theta) + \frac{m}{\sqrt{\rho}}\underline{s}_{\mathrm{III}}(\theta)) \cdot \boldsymbol{n} \\ \text{along the crack faces,} \\ \hat{\underline{\sigma}}^2 \cdot \boldsymbol{n} = -\underline{\tau}(\theta) \cdot \boldsymbol{n} \text{ along the crack faces,} \\ \hat{\boldsymbol{V}}^i \text{ vanishes at infinity.} \end{cases} \tag{10}$$

The system of equations has a unique solution with a finite energy (Leguillon and Sanchez-Palencia 1987) (extension of Lax–Milgram theorem to unbounded domains). As a consequence of the finite energy, the solution decreases to 0 at infinity. The expansion finally writes:

$$\boldsymbol{U}^\ell(x_1, x_2, x_3) = \boldsymbol{U}^\ell(\ell y_1, \ell y_2, \ell y_3) = \boldsymbol{U}^0(0, 0, 0) + K_{\mathrm{I}}\sqrt{\ell}\Big[\sqrt{\rho}u_I(\theta)$$

$$+ m\sqrt{\rho}u_{\mathrm{III}}(\theta) + \hat{V}^1(y_1, y_2, y_3)\Big] + T_3\ell\Big[\rho t(\theta) + \hat{V}^3(y_1, y_2, y_3)\Big] + \ldots \quad (11)$$

The Incremental Energy Release Rate (IERR) is defined as $\mathcal{G}_{\mathrm{inc}} = -\delta W_p/S$, where $W_p = \frac{1}{2}\int_V \underline{\sigma} : \underline{\varepsilon} dV$ is the elastic strain energy and S the crack surface. The elastic strain energy variation due to crack initiation thus writes:

$$-\delta W_p(\ell) = a_{11}(\varphi)K_{\mathrm{I}}^2 + a_{13}(\varphi)K_{\mathrm{I}}K_{\mathrm{III}} + a_{33}(\varphi)K_{\mathrm{III}}^2 + b_1(\varphi)K_{\mathrm{I}}T_3\sqrt{\ell} + b_2(\varphi)K_{\mathrm{III}}T_3\sqrt{\ell} + c(\varphi)T_3^2\ell, \quad (12)$$

where a_{ij}, b_j and c are coefficients depending on the facet shape and angle. The crack surface can be written as $S = \alpha\ell^2$, with α a scaling coefficient depending on the facet shape. As a consequence, the IERR writes:

$$\mathcal{G}_{\mathrm{inc}}(\ell) = -\delta W_p(\ell)/S = \frac{1}{E}\big(A_{11}(\varphi)K_{\mathrm{I}}^2 + A_{13}(\varphi)K_{\mathrm{I}}K_{\mathrm{III}} + A_{33}(\varphi)K_{\mathrm{III}}^2 + B_1(\varphi)K_{\mathrm{I}}T_3\sqrt{\ell} + B_2(\varphi)K_{\mathrm{III}}T_3\sqrt{\ell} + C(\varphi)T_3^2\ell\big), \quad (13)$$

involving the material Young's modulus E and the dimensionless coefficients $A_{ij} = Ea_{ij}/(\alpha\ell^2)$, $B_i = Eb_i/(\alpha\ell^2)$ and $C = Ec/(\alpha\ell^2)$. Introducing the mode mixities m and m_T, the IERR also rewrites:

$$\mathcal{G}_{\mathrm{inc}}(\ell) = \frac{K_{\mathrm{I}}^2}{E}\big[A_{11}(\varphi) + mA_{13}(\varphi) + m^2A_{33}(\varphi) + m_T(\ell)B_1(\varphi) + mm_T(\ell)B_2(\varphi) + m_T(\ell)^2C(\varphi)\big]. \quad (14)$$

We define the dimensionless IERR $\chi = E\mathcal{G}_{\mathrm{inc}}/K_{\mathrm{I}}^2$ so that:

$$\chi(\varphi, m, m_T(\ell)) = A_{11}(\varphi) + mA_{13}(\varphi) + m^2A_{33}(\varphi) + m_T(\ell)B_1(\varphi) + mm_T(\ell)B_2(\varphi) + m_T(\ell)^2C(\varphi). \quad (15)$$

The dimensionless IERR only depends on the Poisson's ratio of the material and on the facet shape.

2.2 Numerical determination of A_{ij}, B_i and C

The functions A_{ij}, B_i and C can be computed in the inner domain as a function of the crack orientation φ. They are obtained by calculating the potential energy difference between configurations with or without crack extensions. It is done by FE calculations (Abaqus quasi-static implicit solver) in the inner domain that is artificially bounded at a distance large with respect to the crack extension (which is 1 in the inner domain). FE calculations are performed under linear elasticity and assuming small deformation in order to calculate the stress and the potential energy release due to crack initiation. The calculations are made in the inner domain including a crack lying in a plane forming an angle φ with the initial crack front. The domain faces in the x_3-direction are inclined with an angle corresponding to the crack angle, which enables modeling an overlap between cracks as proposed in Doitrand and Leguillon (2018). Elliptical crack shapes forming unit radius circular projections in (Oy_1y_2) are considered. Periodic boundary conditions along (Oy_3) direction are imposed on the inner domain lateral faces to represent an infinite network of cracks. The inner domain width thus corresponds to the distance between two facets along (Oy_3) direction. A methodology allowing the determination of the initiation minimum crack spacing was previously proposed (Doitrand and Leguillon 2018; Leguillon and Yosibash 2017). Since we mainly focus on the initiation SIF, the distance between facets is set to 200 times the facet extension along (Ox_1), which is verified to be large enough so that there is no interactions between two facets. If the inter-distance facet is large enough, the IERR does not depends on the facet spacing. However, a smaller IERR is obtained for a facet network with smaller inter-facet spacing so that facet nucleation occurs for a larger imposed loading (Doitrand and Leguillon 2018). The inner domain is artificially bounded at a large distance (200 times the crack extension along (Oy_1) direction) so that a larger domain size results in differences smaller than 2% on the IERR and thus on the loading at crack initiation. Dirichlet boundary conditions based on mode I, mode III and T-stress asymptotic displacement fields corresponding to an initial crack are imposed on the

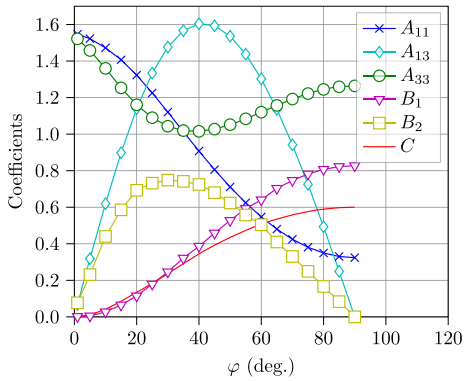

Fig. 3 Variation of the normalized IERR coefficients as a function of the crack orientation obtained for $\nu = 0.36$

inner domain boundary. The mesh, consisting of linear 8-nodes elements, is refined near the facet and typically contains around 1.3 M degrees of freedom. The minimum mesh size near the facet is chosen so that differences in $\mathcal{G}_{\text{inc}}$ smaller than 1% are obtained for a finer mesh. For a given facet angle, three calculations are performed, respectively with prescribed displacements fields corresponding to mode I, mode III and T-stress loading. For each calculation, two steps are performed to obtain the elastic strain energy with and without facet opening, and thus the elastic strain energy variation and IERR. These three calculations enable determining the coefficients $A_{11}(\varphi)$, $A_{33}(\varphi)$ and $C(\varphi)$ [Eq. (15)]. Then, the IERR corresponding to a combination of several modes is obtained by linear combinations of these three calculations, which enables determining the coefficients $A_{13}(\varphi)$, $B_1(\varphi)$ and $B_2(\varphi)$ [Eq. (15)]. The functions A_{ij}, B_i, C are finally computed for different values of φ (Fig. 3).

They only depend on the material Poisson's ratio and facet geometry. In the sequel, a $\nu = 0.36$ Poisson's ratio is used for the calculations. The functions are given for other values of Poisson's ratio in the Appendix.

3 The coupled criterion

3.1 Mode-independent properties

The CC states that crack initiation occurs provided two conditions are fulfilled (Leguillon 2002):

- Stress condition: the tensile stress must be larger than the material tensile strength σ_{c} along the crack path before initiation: $\sigma_{\text{nn}}(\mathbf{x}) \geqslant \sigma_{\text{c}}, \ \forall \ \mathbf{x} \in \Gamma$ (where Γ represents the new crack, i.e. the facet). For the sake of simplicity, in the sequel the stress criterion will be written as $\sigma_{\text{nn}}(\ell) \geqslant \sigma_{\text{c}}$, where ℓ is the facet extension along (Oy_1).
- Energy condition: the potential energy released by crack opening must be larger than the energy required for crack nucleation: $\mathcal{G}_{\text{c}} S$, where $\mathcal{G}_{\text{c}}$ is the material's critical energy release rate (ERR).

The second condition can be written using the IERR defined in Sect. 2.1: $\mathcal{G}_{\text{inc}} = -\delta W_p / S \geqslant \mathcal{G}_{\text{c}}$, which can be calculated using Eq. (14). For a fixed facet orientation with respect to the initial crack φ, applying the CC, $\mathcal{G}_{\text{inc}} \geq \mathcal{G}_{\text{c}}$ and $\sigma_{\text{nn}} \geq \sigma_{\text{c}}$ all along the crack path prior to initiation, reverts to determining the facet nucleation SIF $K_{\text{I}}(\varphi)$ and the corresponding crack extension $\ell_{\text{c}}(\varphi)$. They are obtained by solving the following equation system:

$$\begin{cases} \frac{K_{\text{I}}^2}{E} \chi(\varphi, m, m_T(\ell_{\text{c}})) \geqslant \mathcal{G}_{\text{c}}, \\ \frac{K_{\text{I}}}{\sqrt{\ell}} (s_{nn}^{\text{I}}(\varphi) + m s_{nn}^{\text{III}}(\varphi) + m_T(\ell) \tau_{nn}(\varphi)) \geqslant \sigma_{\text{c}}. \end{cases} \tag{16}$$

For each value of φ, combining both equations finally yields the equation that must be solved to determine the initiation crack length ℓ_{c}:

$$\frac{\chi(\varphi, m, m_T(\ell_{\text{c}}))}{(s_{nn}^{\text{I}}(\varphi) + m s_{nn}^{\text{III}}(\varphi) + m_T(\ell_{\text{c}}) \tau_{nn}(\varphi))^2} = \frac{1}{\ell_{\text{c}}} \frac{E \mathcal{G}_{\text{c}}}{\sigma_{\text{c}}^2} \tag{17}$$

Introducing the material characteristic length $\ell_{\text{mat}} = \frac{E \mathcal{G}_{\text{c}}}{\sigma_{\text{c}}^2}$, it can be deduced from Eq. (17) that the same initiation length ℓ_{c} is obtained for different material properties resulting in a similar ℓ_{mat}. Equation (17) can be solved using Newton's method to determine $\ell_{\text{c}}(\varphi)$. The SIF to initiate a facet oriented with an angle φ is then obtained as:

$$K_{\text{I}}(\varphi) = \sqrt{\frac{E \mathcal{G}_{\text{c}}}{\chi(\varphi, m, m_T(\ell_{\text{c}}(\varphi)))}}, \tag{18}$$

or equivalently by:

$$K_{\text{I}}(\varphi) = \frac{\sigma_{\text{c}} \sqrt{\ell_{\text{c}}(\varphi)}}{s_{nn}^{\text{I}}(\varphi) + m s_{nn}^{\text{III}}(\varphi) + m_T(\ell_{\text{c}}(\varphi)) \tau_{nn}(\varphi)}. \tag{19}$$

In the sequel, we refer to $K_{\mathrm{I}}(\varphi)$ as facet nucleation SIF. The first facet to initiate corresponds to the one oriented with an angle φ_{c} that requires the smallest facet nucleation SIF, facet initiation thus occurs for a facet nucleation apparent SIF $K_{\mathrm{I}}^{\mathrm{app}}$:

$$\begin{cases} K_{\mathrm{I}}^{\mathrm{app}} = \min\limits_{\varphi}(K_{\mathrm{I}}(\varphi)), \\ \varphi_{\mathrm{c}} = \arg\min\limits_{\varphi}(K_{\mathrm{I}}(\varphi)). \end{cases} \tag{20}$$

For a given mode mixity $\beta = K_{\mathrm{III}}/(K_{\mathrm{I}} + |K_{\mathrm{III}}|)$, the corresponding mode III apparent SIF can be obtained as $K_{\mathrm{III}} = (\beta/(1-\beta))K_{\mathrm{I}}$. In the case of pure mode III loading, $\beta = 1$ ($K_{\mathrm{I}} = 0$) and the same reasoning as previously can be employed by replacing K_{I} by K_{III}.

3.2 Mode-dependent properties

We now consider opening and shear mixed mode crack initiation. It consists in introducing the material shear strength (τ_{c}) and critical ERR ($\mathcal{G}_{\mathrm{IIIc}}$) in the stress and energy conditions respectively. These parameters are generally not used for isotropic homogeneous material since even under shear loading, the crack takes an orientation so that it is loaded under opening mode. They are more usually encountered when dealing with interface failure, where they are defined as the strength and critical ERR corresponding to straight crack propagation along the interface under remote pure antiplane shear. The same definition can be kept in the case of isotropic homogeneous material. The parameters τ_{c} and $\mathcal{G}_{\mathrm{IIIc}}$ are thus defined as the theoretical strength and critical ERR that would correspond to a straight crack propagation under remote pure antiplane shear. Of course, this configuration is not achieved in experiments. However, it can be encountered numerically using models such as the CC in which the crack path is a priori defined, thus possibly experiencing both opening and shear.

It is expected that if the loading is not pure opening, not only the tensile strength σ_{c} and critical ERR $\mathcal{G}_{\mathrm{Ic}}$ are involved but also τ_{c} and rate $\mathcal{G}_{\mathrm{IIIc}}$. It is thus possible to rewrite the stress and the energy criteria in a very general way that accounts for the stress mixity in the fracture mechanism. The mixed mode CC formulation was established in 2D to study crack initiation under mode I+II+T-stress loading (Leguillon and Murer 2008). We extend this formulation to 3D for mode I+III+T-stress loading. We start rewriting the stress criterion to account for the stress mixity, which writes:

$$\begin{cases} \sigma_{\mathrm{nn}}(r,\theta) = \frac{K_{\mathrm{I}}}{\sqrt{r}}\Big(s_{nn}^{\mathrm{I}}(\theta) \\ \quad + m s_{nn}^{\mathrm{III}}(\theta) + m_T(r)\tau_{nn}(\theta) + \ldots\Big), \\ \sigma_{\mathrm{nt}}(r,\theta) = \frac{K_{\mathrm{I}}}{\sqrt{r}}\Big(s_{\mathrm{nt}}^{\mathrm{I}}(\theta) \\ \quad + m s_{\mathrm{nt}}^{\mathrm{III}}(\theta) + m_T(r)\tau_{\mathrm{nt}}(\theta) + \ldots\Big), \end{cases} \tag{21}$$

where σ_{nn} and σ_{nt} respectively hold for the tensile and out-of-plane shear components of the stress tensor, m and m_T are the previously defined mixity parameters. The functions $s_{\mathrm{nn}}^{\mathrm{i}}$, $s_{\mathrm{nt}}^{\mathrm{i}}$ and τ_{nt}^{i} are calculated analytically and shown in Fig. 4 for $\nu = 0.36$.

We define a mixity parameter μ based on the shear and tensile stress components:

$$\mu = \frac{|\sigma_{\mathrm{nt}}|}{\sigma_{\mathrm{nn}}}, \tag{22}$$

which varies between 0 (pure opening mode) and ∞ (pure shear mode). The stress mixity $\psi = \tan^{-1}(\mu)$ may also be used, which thus varies between 0 (pure opening mode) and $\pi/2$ (pure shear mode). The energy criterion is written based on Hutchinson's and Suo's condition (1992) so that the critical ERR is defined as a function of opening ($\mathcal{G}_{\mathrm{Ic}}$) and shear ($\mathcal{G}_{\mathrm{IIIc}}$) critical ERR and stress mixity:

$$\begin{cases} \mathcal{G}_{\mathrm{c}}(\psi) = \mathcal{G}_{\mathrm{Ic}}(1 + \tan^2(\xi\psi)), \\ \text{with } \xi = \frac{2}{\pi}\tan^{-1}\left(\sqrt{\frac{\mathcal{G}_{\mathrm{IIIc}}}{\mathcal{G}_{\mathrm{Ic}}} - 1}\right). \end{cases} \tag{23}$$

For pure opening mode, $\psi = 0$ and $\mathcal{G}_{\mathrm{c}} = \mathcal{G}_{\mathrm{Ic}}$ whereas for pure shear mode, $\psi = \pi/2$ and $\mathcal{G}_{\mathrm{c}} = \mathcal{G}_{\mathrm{IIIc}}$. The local shear and tensile stress components may not be uniform over the whole crack surface before initiation, which results in varying stress mixity and thus varying $\mathcal{G}_{\mathrm{c}}$ over the whole crack surface before initiation. As a consequence, we define $\overline{\mathcal{G}}_{\mathrm{c}}$ as the average critical ERR over the crack surface before initiation, which writes:

$$\overline{\mathcal{G}}_{\mathrm{c}}(\ell) = \frac{1}{S}\int_{\Gamma} \mathcal{G}_{\mathrm{c}}(\psi)dS, \tag{24}$$

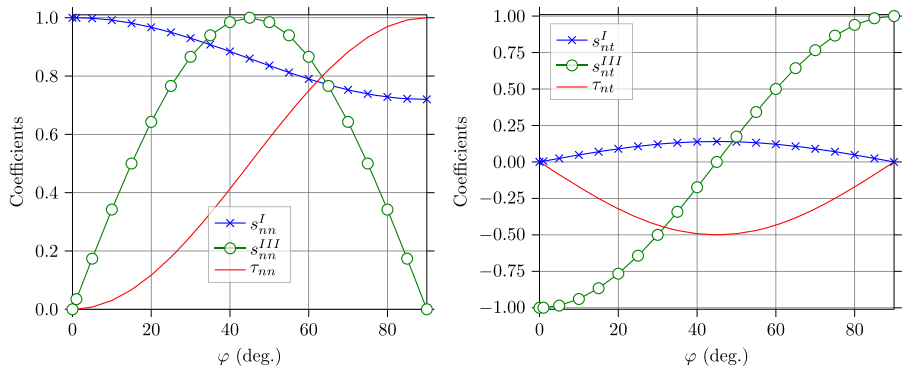

Fig. 4 Variation of the normalized **a** tensile and **b** shear stress components as a function of the crack orientation

where Γ represents the crack and S represents the crack surface (area $S = \alpha\ell^2$). The variable $\overline{\mathcal{G}}_c$ thus depends on the crack extension along (Ox_1) direction, ℓ. The energy condition of the CC considering mode-dependent fracture properties writes:

$$\mathcal{G}_{inc}(\ell) \geqslant \overline{\mathcal{G}}_c(\ell) \tag{25}$$

The stress criterion, which must be fulfilled over Γ, is written as a power ellipse surface in the tensile-shear stress space (in the following, we consider $q = 2$):

$$\left(\frac{\sigma_{nn}(\ell)}{\sigma_c}\right)^q + \left(\frac{\sigma_{nt}(\ell)}{\tau_c}\right)^q \geqslant 1, \tag{26}$$

which rewrites in the following form:

$$\sigma_{nn}(\ell) \geqslant \frac{\sigma_c\tau_c}{\left(\tau_c^q + \mu(\ell)^q\sigma_c^q\right)^{1/q}}. \tag{27}$$

Combining both energy and stress conditions finally leads to the following system of equations to be solved:

$$\begin{cases} \frac{K_I^2}{E}\chi(\varphi, m, m_T(\ell)) \geqslant \overline{\mathcal{G}}_c(\ell), \\ \frac{K_I}{\sqrt{\ell}}\left(s^I_{nn}(\varphi) + m s^{III}_{nn}(\varphi) + m_T(\ell)\tau_{nn}(\varphi)\right) \\ \quad \geqslant \frac{\sigma_c\tau_c}{\left(\tau_c^q + \mu(\ell)^q\sigma_c^q\right)^{1/q}}, \end{cases} \tag{28}$$

which leads to the implicit equation that must be solved for a fixed φ to determine the initiation crack extension $\ell_c(\varphi)$:

$$\frac{\chi(\varphi, m, m_T(\ell_c))}{\left(s^I_{nn}(\varphi) + m s^{III}_{nn}(\varphi) + m_T(\ell_c)\tau_{nn}(\varphi)\right)^2}$$

$$= \frac{1}{\ell_c}\frac{E\overline{\mathcal{G}}_c(\ell_c)\left(\tau_c^q + \mu(\ell_c)^q\sigma_c^q\right)^{2/q}}{\sigma_c^2\tau_c^2}. \tag{29}$$

The facet nucleation SIF, i.e. the SIF corresponding to the initiation of a facet with angle φ finally writes:

$$K_I(\varphi) = \sqrt{\frac{E\overline{\mathcal{G}}_c(\ell_c(\varphi))}{\chi(\varphi, m, m_T(\ell_c(\varphi)))}}. \tag{30}$$

Finally, the initiation angle φ_c and facet nucleation apparent SIF K_I^{app} are obtained by minimization of $K_I(\varphi)$.

$$\begin{cases} K_I^{app} = \min_{\varphi}(K_I(\varphi)), \\ \varphi_c = \arg\min_{\varphi}(K_I(\varphi)). \end{cases} \tag{31}$$

4 Results for mode-independent properties

We recall that an objective of this work is to evaluate conditions for which facet nucleation may occur instead of straight crack propagation for different values of the mode mixity β. Facet nucleation is likely to occur provided the facet nucleation apparent SIF is smaller than straight crack propagation apparent SIF. In this section, we thus assess straight crack propagation and facet nucleation under mode I+III in presence or not of T-stress, considering mode-independent fracture properties.

4.1 Straight crack propagation

In the case of straight crack propagation under mode I and III loading, the crack propagates when $\mathcal{G} = K_I^2(1-$

$\nu^2)/E + K_{\mathrm{III}}^2(1+\nu)/E = \mathcal{G}_{\mathrm{c}}$. Therefore, the apparent SIF $K_{\mathrm{I}}^{\mathrm{app}}$ at which the crack propagates writes as a function of the mode mixity β:

$$K_{\mathrm{I}}^{\mathrm{app}} = \sqrt{\frac{E\mathcal{G}_{\mathrm{c}}}{1-\nu^2+\left(\frac{\beta}{1-\beta}\right)^2(1+\nu)}} \tag{32}$$

$K_{\mathrm{I}}^{\mathrm{app}}$ is equal to the material's critical SIF ($K_{\mathrm{Ic}} = \sqrt{E\mathcal{G}_{\mathrm{Ic}}/(1-\nu^2)}$) for a straight crack propagating under pure mode I loading. Facet nucleation occurs provided the facet nucleation apparent SIF is smaller than straight crack propagation apparent SIF.

4.2 Mode I+III

The CC is applied to study facet nucleation under mode I+III in absence of T-stress ($T_3/\sigma_{\mathrm{c}} = 0$). Figure 5 shows normalized facet nucleation SIF [Eq. (18)] variation as a function of the facet angle for different mode mixities increasing from pure mode I (top) to pure mode III (bottom).

Whatever the mode mixity, χ (and thus $K_{\mathrm{I}}^{\mathrm{app}}$, see Eq.18) does not depend on ℓ under mode I+III if $T_3/\sigma_{\mathrm{c}} = 0$ [Eq. (15)]. As a consequence, facet nucleation apparent SIF only depends on the energy criterion. Figure 5b shows facet nucleation angle (Eq. 20) as a function of the mode mixity. For sufficiently small (close to mode I, $\beta \leqslant 0.1$) or sufficiently large (close to mode III, $\beta \geqslant 0.8$) mode mixities, the most favorable crack propagation angle is zero, i.e. in the initial crack direction. This is due to A_{11} and A_{33} exhibiting a maximum for $\varphi = 0°$ (Fig. 3). For intermediate mixities ($0.1 \leqslant \beta \leqslant 0.8$), the most favorable facet angle lies between 0° and 28° (maximum attained for $\beta \approx 0.6$). Figure 6 shows normalized facet extension along (Ox_1) direction obtained from Eq. (17) and facet nucleation apparent SIF [Eq. (20)] as a function of the mode mixity.

Whatever the mode mixity, facet nucleation apparent SIF is larger than straight crack propagation apparent SIF [Eq. (32)]. It means that facet nucleation is less favorable than straight crack propagation. Therefore, supplementary ingredients are needed to explain why crack front segmentation is observed experimentally.

4.3 Mode I+III+T-stress

We now consider the influence of a T-stress component parallel to the initial crack front on facet nucleation for several values of the mode mixity β. Figure 7a shows the normalized facet nucleation SIF [Eq. (18)] as a function of the facet angle for $\beta = 0$ mode mixity (i.e. mode I+T-stress loading) and different T-stress magnitudes.

For sufficiently small T-stress magnitudes, the facet nucleation apparent SIF (indicated as a circle for a given T-stress magnitude on Fig. 7a) is obtained for $\varphi = 0°$. facet angle corresponding to a propagation in the initial crack direction. However, for normalized T-stress magnitudes $T_3/\sigma_{\mathrm{c}} > 0.02$, facets initiate with a $\varphi = 90°$ angle which actually corresponds to failure being induced by T-stress (Fig. 7b). Figure 7c shows the normalized facet nucleation apparent SIF [Eq. (20)] as a function of the normalized T-stress. It highlights that facet nucleation becomes more favorable than straight crack propagation for sufficiently large T-stress magnitudes.

Figure 8a shows the normalized facet nucleation SIF [Eq. (18)] as a function of the facet angle for $\beta = 0.5$ mode mixity and different T-stress magnitudes.

Whatever the T-stress magnitude, the SIF variation as a function of the facet angle exhibits a minimum corresponding to the facet initiation angle varying between 26° and 90° when increasing the T-stress magnitude (Fig. 8b). For T_3/σ_{c} larger than 0.1, facet nucleation becomes more favorable than straight crack propagation since facet nucleation apparent SIF becomes smaller than straight crack propagation apparent SIF.

Therefore, a first ingredient that has an influence on the facet nucleation apparent SIF and angle is the non-singular T-stress acting parallel to the crack front direction. A sufficiently large T-stress magnitude actually promotes facet initiation rather than straight crack propagation. Nevertheless, the resulting facet angles are large compared to those measured experimentally (Cambonie and Lazarus 2014; Chen et al. 2015; Eberlein et al. 2017; Pham and Ravi-Chandar 2014, 2016).

5 Results for mode-dependent properties

In this section, we study the influence of considering mode-dependent fracture properties on both straight crack propagation and facet nucleation in the absence of T-stress.

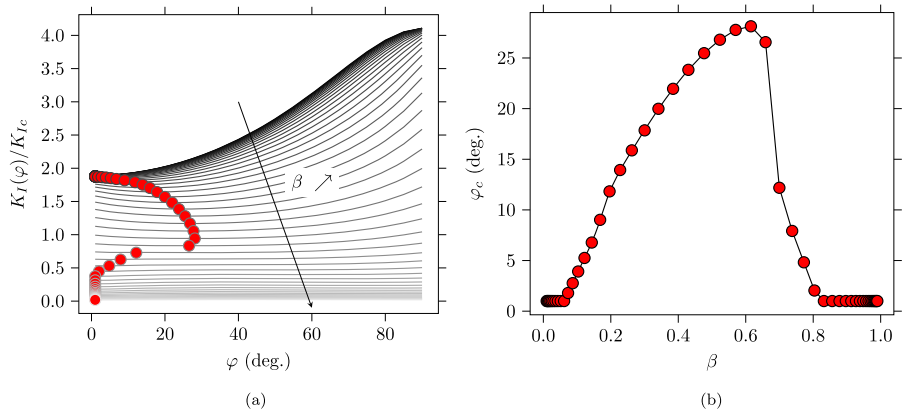

Fig. 5 **a** Normalized facet nucleation SIF as a function of the facet angle for several mode mixities (circles represent the facet nucleation apparent SIF, i.e. the minimum SIF for a given mixity) and **b** Initiation facet angle (minimizing normalized facet nucleation SIF) as a function of the mode mixity

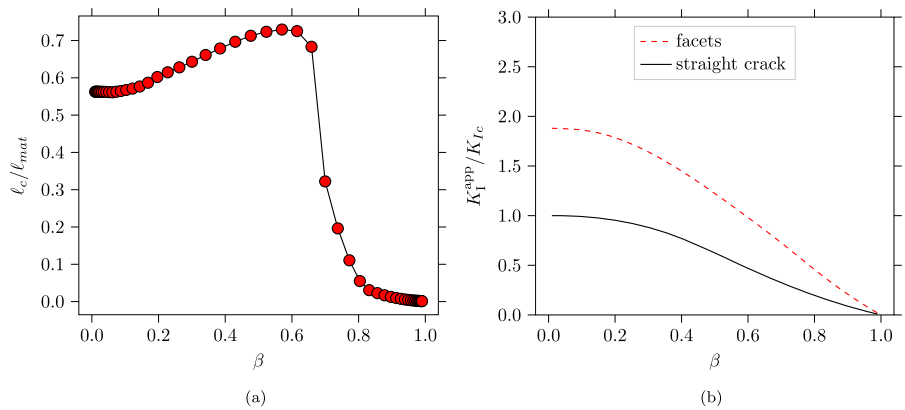

Fig. 6 Normalized **a** initiation facet extension along (Ox_1) direction and **b** apparent SIF corresponding either to facet nucleation (dashed line) or straight crack propagation (plain line) as a function of the mode mixity

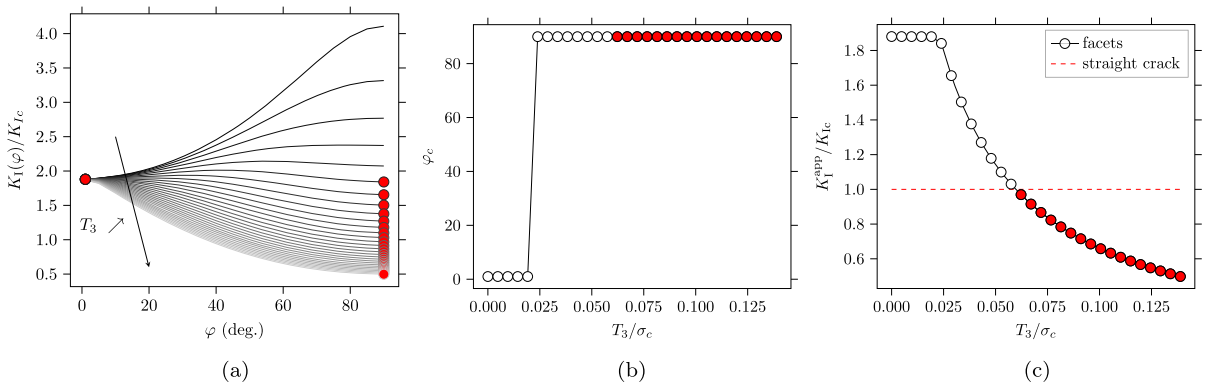

Fig. 7 Normalized **a** facet nucleation SIF variation as a function of facet angle (circles correspond to the minimum SIF for a given T-stress), **b** initiation facet angle and **c** facet nucleation apparent SIF as a function of normalized T-stress for $\beta = 0$. Filled circles in **b** and **c** correspond to configurations for which facet initiation is more favorable than straight crack propagation

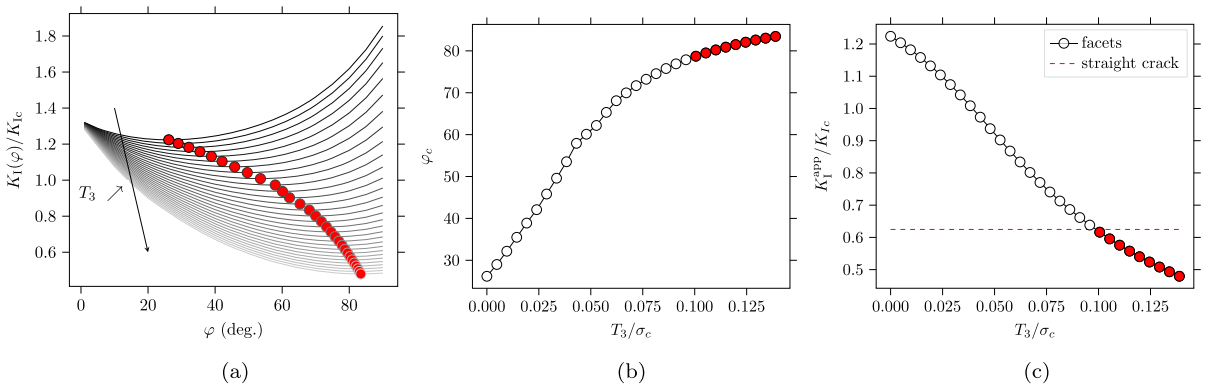

Fig. 8 Normalized **a** facet nucleation SIF variation as a function of facet angle (circles correspond to the minimum SIF for a given T-stress), **b** initiation facet angle and **c** facet nucleation apparent SIF as a function of normalized T-stress for $\beta = 0.5$. Filled circles in **b** and **c** correspond to configurations for which facet initiation is more favorable than straight crack propagation

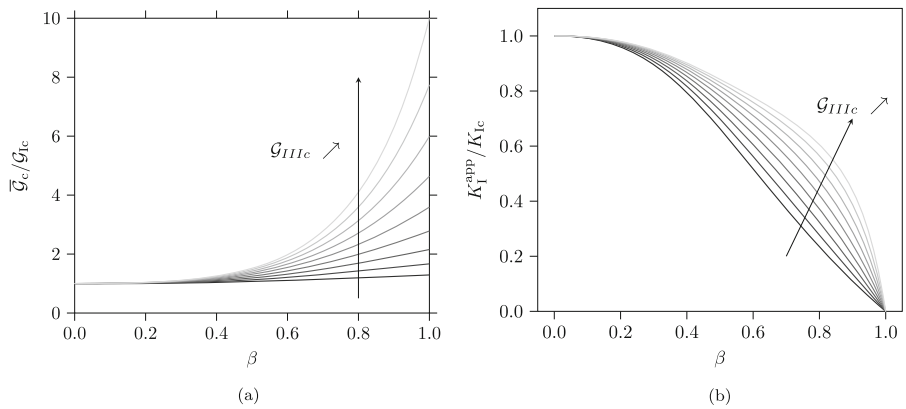

Fig. 9 Normalized **a** average critical ERR as a function of the mode mixity and **b** straight crack propagation apparent SIF for several shear critical ERR

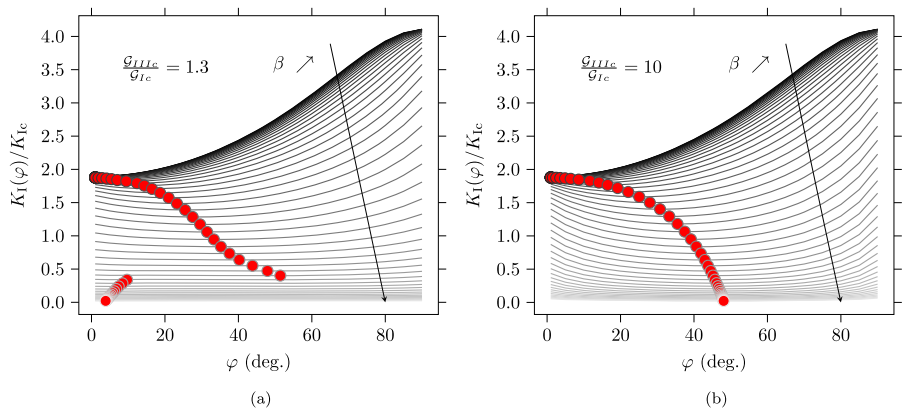

Fig. 10 Normalized facet nucleation SIF as a function of facet angle for **a** $\mathcal{G}_{IIIc}/\mathcal{G}_{Ic} = 1.3$ and **b** $\mathcal{G}_{IIIc}/\mathcal{G}_{Ic} = 10$ for several mode mixities

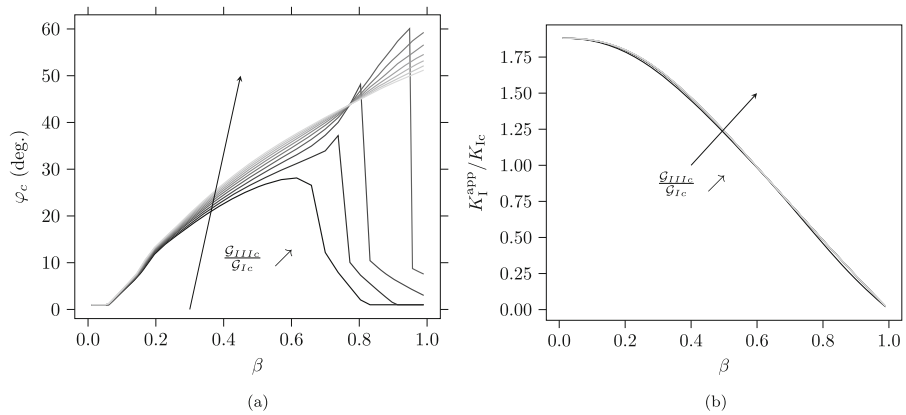

Fig. 11 **a** Facet nucleation angle and **b** normalized facet nucleation apparent SIF variation as a function of the mode mixity for shear to opening critical ERR ratios between 0 and 15

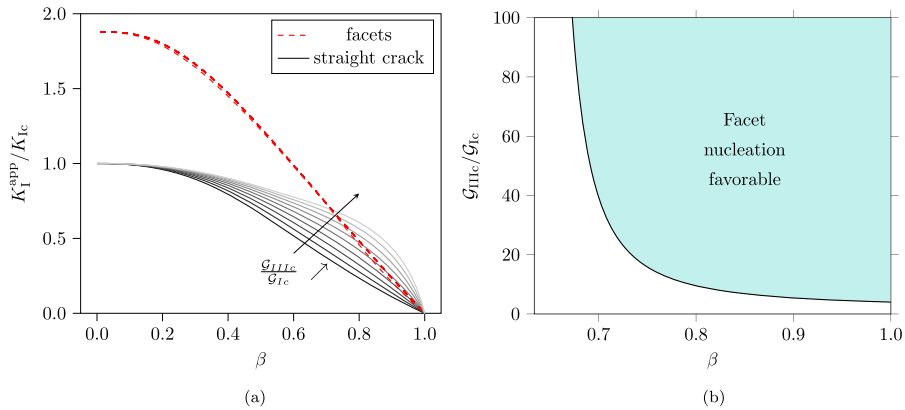

Fig. 12 Normalized **a** facet nucleation and straight propagation apparent SIF for several shear to opening critical ERR ratios and **b** shear to opening critical ERR ratio as a function of the mode mixity highlighting configurations for which facet nucleation is more favorable than straight crack propagation

5.1 Straight crack propagation

The straight crack propagation apparent SIF considering mode-dependent properties is obtained by replacing $\mathcal{G}_c$ by $\overline{\mathcal{G}}_c$ into Eq. (32):

$$K_I^{app} = \sqrt{\frac{E\overline{\mathcal{G}}_c}{1-\nu^2+\left(\frac{\beta}{1-\beta}\right)^2(1+\nu)}} \tag{33}$$

Mode-dependent properties are thus considered by varying the critical ERR between the pure opening ($\mathcal{G}_{Ic}$) and shear ($\mathcal{G}_{IIIc}$) values depending on the local stress mixity $\mu = \frac{|\sigma_{nt}|}{\sigma_{nn}}$ [Eq. (23)]. In the case of straight crack propagation, the stress mixity is $\mu = \frac{|K_{III}|}{K_I} = \frac{\beta}{1-\beta}$[or equivalently $\psi = \tan^{-1}(\mu) = \tan^{-1}\left(\frac{\beta}{1-\beta}\right)$]. It yields, using Eq. (23):

$$\begin{cases} \mathcal{G}_c = \mathcal{G}_{Ic}\left\{1+\tan^2\left\{\xi\tan^{-1}\left(\frac{\beta}{1-\beta}\right)\right\}\right\}, \\ \xi = \frac{2}{\pi}\tan^{-1}\left(\sqrt{\frac{\mathcal{G}_{IIIc}}{\mathcal{G}_{Ic}}}-1\right). \end{cases} \tag{34}$$

Figure 9a shows the normalized average critical ERR [Eq. (24)] variations as a function of the mode mixity for different $\mathcal{G}_{IIIc}$ values [Eq. (34)].

The stress mixity increases when increasing the mode mixity, which also increases the average critical ERR. As a consequence, a larger straight crack propagation apparent SIF [Eq. (33)] is obtained considering mode-dependent fracture properties (Fig. 9b). Considering mode-dependent fracture properties induces only a small increase in straight crack propagation apparent SIF for small mode mixities since the stress mixity results in a moderate increase in $\mathcal{G}_c$, not sufficient to make facet nucleation favorable (Fig. 6b). However, for larger mode mixities, the larger stress mixity induces a larger increase in $\mathcal{G}_c$ and thus in straight crack propagation apparent SIF. As a consequence, facet nucleation may become possible provided the straight crack propagation apparent SIF overcomes the facet nucleation apparent SIF, which is assessed in the sequel.

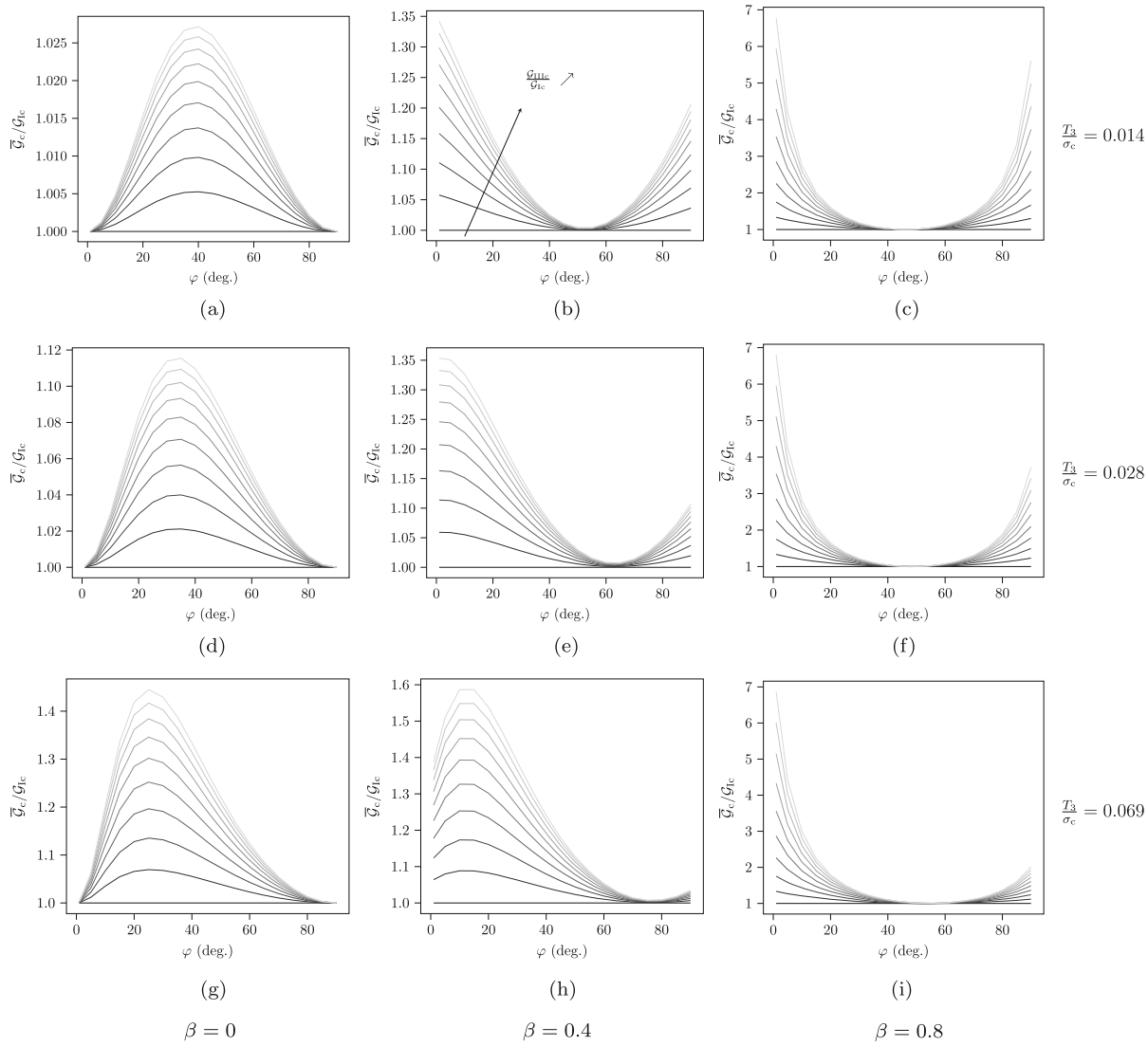

Fig. 13 Normalized average critical ERR as a function of facet angle obtained for $\mathcal{G}_{IIIc}/\mathcal{G}_{Ic}$ ratios between 1 and 50, **a**–**c** $T_3/\sigma_c = 0.014$, **d**–**f** $T_3/\sigma_c = 0.028$ and **a**–**c** $T_3/\sigma_c = 0.069$ normalized T-stress magnitudes and **a**, **d**, **g** $\beta = 0$, **b**, **e**, **h** $\beta = 0.4$ or **c**, **f**, **i** $\beta = 0.8$ mode mixities

5.2 Mode I+III

Figure 10a and b shows normalized facet nucleation SIF [Eq. (30)] as a function of facet angle under mode I+III considering mode-dependent properties for $\mathcal{G}_{IIIc}/\mathcal{G}_{Ic} = 1.3$ or 10. For each value of β, the face nucleation apparent SIF, obtained for a facet angle minimizing the facet nucleation SIF [Eq. (31)] is depicted by a circle. For $\mathcal{G}_{IIIc}/\mathcal{G}_{Ic}$ smaller than 1.5 (Fig. 10a), for sufficiently small (close to mode I, $\beta \leqslant 0.1$) or sufficiently large mode mixities, the most favorable crack propagation angle is close to zero, i.e. in the initial crack direction. This is due to A_{11} and A_{33} exhibiting a maximum for $\varphi = 0°$ (Fig. 3). For intermediate mixities ($0.1 \leqslant \beta \leqslant 0.8$), the most favorable facet angle lies between 0° and a maximum value depending on $\mathcal{G}_{IIIc}/\mathcal{G}_{Ic}$. For $\mathcal{G}_{IIIc}/\mathcal{G}_{Ic}$ larger than 1.5 (Fig. 10b), the facet nucleation angle varies monotonically with increasing mode mixity. The facet nucleation angle and

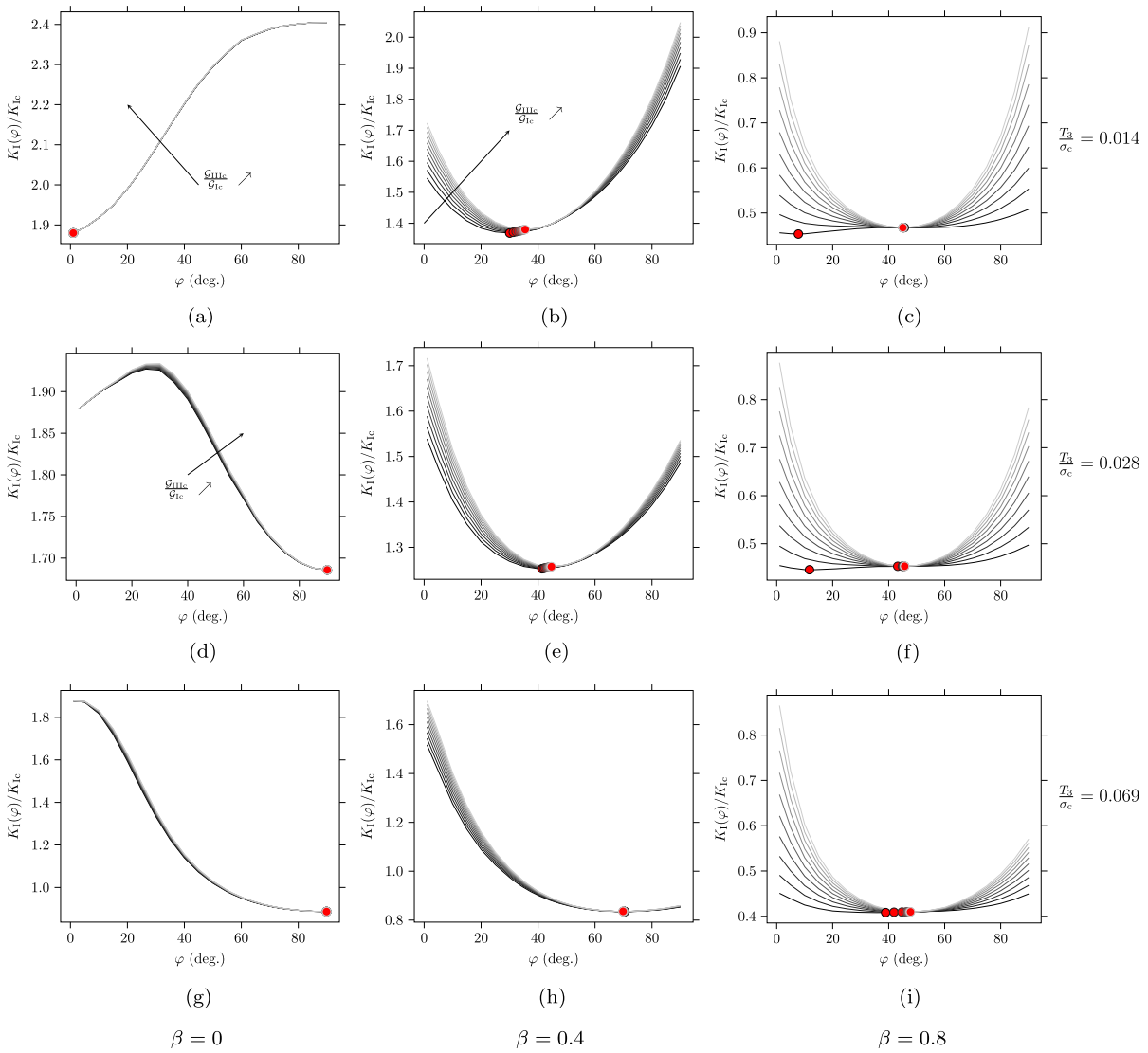

Fig. 14 Normalized facet nucleation SIF variation as a function of facet angle obtained for $\mathcal{G}_{IIIc}/\mathcal{G}_{Ic}$ ratios between 1 and 50, for **a**–**c** $T_3/\sigma_c = 0.014$, **d**–**f** $T_3/\sigma_c = 0.028$ and **a**–**c** $T_3/\sigma_c = 0.069$ normalized T-stress magnitudes and **a**, **d**, **g** $\beta = 0$, **b**, **e**, **h** $\beta = 0.4$ or **c**, **f**, **i** $\beta = 0.8$ mode mixities

apparent SIF are shown in Fig. 11 as a function of the mode mixity for several values of $\mathcal{G}_{IIIc}/\mathcal{G}_{Ic}$.

For $\beta \leqslant 0.2$, increasing $\mathcal{G}_{IIIc}$ does not influence facet nucleation apparent initiation angle. However, for larger β, it tends to shift the SIF minimum to larger facet angles so that for $\mathcal{G}_{IIIc}/\mathcal{G}_{Ic}$ larger than 1.5, facet nucleation angle varies monotonously as a function of β between 0° (pure mode I) and $\approx$ 45–60° (pure mode III). Nevertheless, the facet nucleation apparent SIF is only slightly modified by considering larger $\mathcal{G}_{IIIc}$ except for large mode mixity values (Fig. 11b).

5.3 Comparison between straight crack propagation and facet nucleation

Facet nucleation [Eq. (31)] and straight crack propagation [Eq. (33)] apparent SIF are finally compared as function of the mode mixity for several $\mathcal{G}_{IIIc}/\mathcal{G}_{Ic}$ ratios,

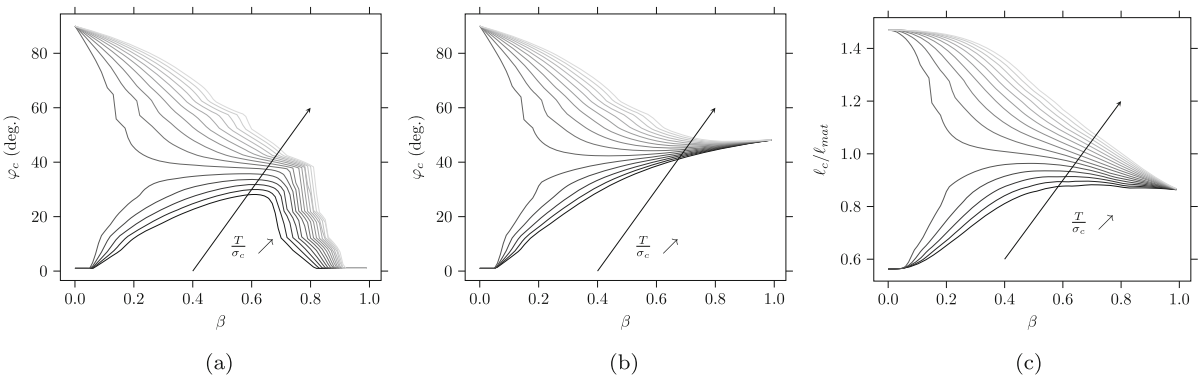

Fig. 15 **a**, **b** Facet nucleation angle and **c** normalized initiation length as a function of the mode mixity for different T-stress magnitudes for **a** $\mathcal{G}_{\mathrm{IIIc}}/\mathcal{G}_{\mathrm{Ic}} = 1$, and **b**, **c** $\mathcal{G}_{\mathrm{IIIc}}/\mathcal{G}_{\mathrm{Ic}} = 10$

considering mode-dependent properties in absence of T-stress ($T_3/\sigma_c = 0$), in Fig. 12a.

Whatever $\mathcal{G}_{\mathrm{IIIc}}/\mathcal{G}_{\mathrm{Ic}}$, straight crack propagation remains more favorable than facet nucleation for mode mixities smaller than $\beta \approx 0.63$ (or equivalently $|K_{\mathrm{III}}|/K_{\mathrm{I}} > 1.7$). For larger mode mixities, facet nucleation may become more favorable than straight crack propagation provided $\mathcal{G}_{\mathrm{IIIc}}/\mathcal{G}_{\mathrm{Ic}}$ is large enough. The configurations for which facet nucleation is more favorable are depicted in Fig. 12b as a function of $\mathcal{G}_{\mathrm{IIIc}}/\mathcal{G}_{\mathrm{Ic}}$ and β. For a fixed $\mathcal{G}_{\mathrm{IIIc}}/\mathcal{G}_{\mathrm{Ic}}$, it enables determining a $|K_{\mathrm{III}}|/K_{\mathrm{I}}$ threshold above which facet nucleation becomes favorable. Therefore, considering mode-dependent properties provides an explanation for facet nucleation being more favorable than straight crack propagation. However, it is not sufficient to explain all the experimental observations since it is limited to large enough mode mixities ($\beta > 0.63$ or equivalently $K_{\mathrm{III}}/K_{\mathrm{I}} > 1.7$).

6 Results considering both T-stress and mode-dependent properties

We finally analyze the combined influence of both mode-dependent properties and T-stress on facet nucleation. Figure 13 shows the normalized average critical ERR [Eq. (24)] as a function of facet angle obtained for several T-stress magnitudes, mode mixities and $\mathcal{G}_{IIIc}$.

The variable $\overline{\mathcal{G}}_{\mathrm{c}}$ varies between $\mathcal{G}_{\mathrm{Ic}}$ if the crack is loaded under pure opening and $\mathcal{G}_{\mathrm{IIIc}}$ if the crack is loaded under pure antiplane shear. For instance, in absence of mode III contribution (Fig. 13a, d, g), $\overline{\mathcal{G}}_{\mathrm{c}} = \mathcal{G}_{\mathrm{Ic}}$ for $\varphi = 0°$ or $\varphi = 90°$ and slightly increases for intermediate angles, the maximum value depending on the magnitude of T-stress inducing antiplane shear depending on the facet angle. Mode III contributes to increase antiplane shear especially for facet angles close to 0° and 90°, which thus increases the corresponding $\overline{\mathcal{G}}_{\mathrm{c}}$ (Fig. 13b, e, h and c, f, i). Increasing the T-stress magnitude tends to shift the angle for which the facet is mainly loaded under opening mode, i.e. for which $\overline{\mathcal{G}}_{\mathrm{c}}$ is minimum.

Figure 14 shows normalized facet nucleation SIF [Eq. (30)] variation as a function of facet angle considering different T-stress magnitudes, mode mixities and mode-dependent properties.

For mode I loading (Fig. 14a, d, g), facet nucleation SIF is almost not influenced by mode-dependent fracture properties. Increasing the T-stress magnitude induces a SIF minimum switch from 0 to 90°, i.e. from crack propagation in the initial crack direction to facet nucleation perpendicularly to the initial crack front. For mode I+III loading (Fig. 14b, e, h and c, f, i), mode-dependent properties induce a change in facet nucleation SIF variation so that the facet nucleation SIF increases for facet angles for which the crack experiences shear (corresponding to larger average critical ERR, see Fig. 13). The larger the mode mixity, the larger the change in facet nucleation SIF due to mode-dependent fracture properties, which induces a moderate change in the facet nucleation SIF minimum (i.e. the facet nucleation apparent SIF) and corresponding angle for intermediate mode mixities ($\beta = 0.4$, Fig. 14b, e, h) and significant changes for larger mode mixities ($\beta = 0.8$, Fig. 14c, f, i). Increasing the T-stress magnitudes tends to increase the facet nucleation angle.

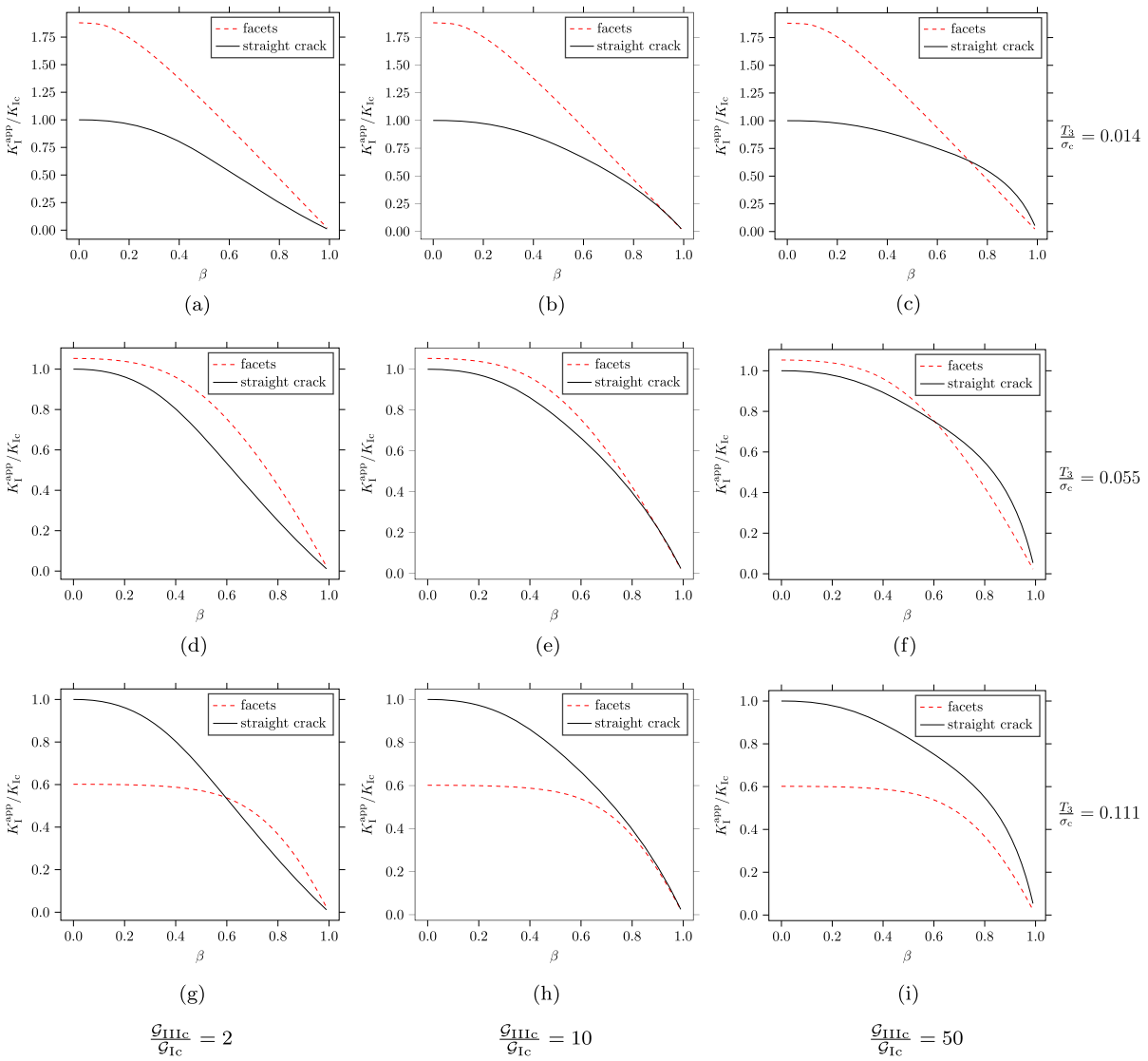

Fig. 16 Normalized facet nucleation (dashed line) and straight crack propagation (plain line) apparent SIF as a function of the mode mixity obtained for **a–c** $T_3/\sigma_c = 0.014$, **d–f** $T_3/\sigma_c = 0.055$ and **g–i** $T_3/\sigma_c = 0.111$ and **a**, **d**, **g** $\mathcal{G}_{\mathrm{IIIc}}/\mathcal{G}_{\mathrm{Ic}} = 2$, **b**, **e**, **h** $\mathcal{G}_{\mathrm{IIIc}}/\mathcal{G}_{\mathrm{Ic}} = 10$ and **c**, **f**, **i** $\mathcal{G}_{\mathrm{IIIc}}/\mathcal{G}_{\mathrm{Ic}} = 50$

Figure 15 shows the facet nucleation angle [Eq. (31)] and normalized facet extension along (Ox_1) direction variations as a function of the mode mixity obtained for different T-stress magnitudes and $\mathcal{G}_{\mathrm{IIIc}}/\mathcal{G}_{\mathrm{Ic}}$ ratios.

For small mode mixities, failure either occurs by crack propagation in the direction of the initial crack ($\varphi = 0°$) or by facet nucleation due to T-stress ($\varphi = 90°$). For increasing mode mixities, the range of facet nucleation angles obtained for several T-stress magnitudes decreases (Fig. 15a, b). Similarly, the normalized initiation crack length range decreases with increasing mode mixity and takes different values depending on failure being triggered by crack propagation ($\ell_c/\ell_{\mathrm{mat}} \approx 0.55$) in the initial direction of facet nucleation due to T-stress ($\ell_c/\ell_{\mathrm{mat}} \approx 1.5$) (Fig. 15c).

Configurations for which facet nucleation occurs can be determined by comparing facet nucleation SIF to straight crack propagation SIF for different mode

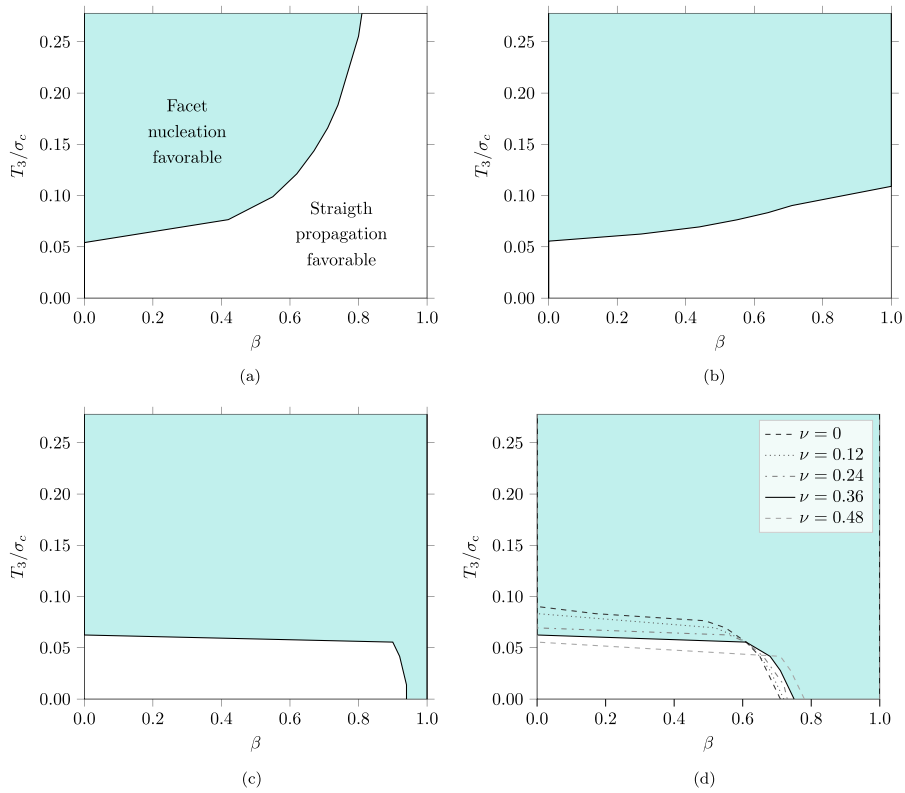

Fig. 17 Domains in the normalized T-stress as a function of the mode mixity space corresponding to facet nucleation or straight crack propagation for **a** $\mathcal{G}_{\mathrm{IIIc}}/\mathcal{G}_{\mathrm{Ic}} = 2$, **b** $\mathcal{G}_{\mathrm{IIIc}}/\mathcal{G}_{\mathrm{Ic}} = 8$, **c** $\mathcal{G}_{\mathrm{IIIc}}/\mathcal{G}_{\mathrm{Ic}} = 10$ and **d** $\mathcal{G}_{\mathrm{IIIc}}/\mathcal{G}_{\mathrm{Ic}} = 50$

mixities, T-stress magnitudes and $\mathcal{G}_{\mathrm{IIIc}}/\mathcal{G}_{\mathrm{Ic}}$ ratios, see Fig. 16. Straight crack propagation remains more favorable than facet nucleation whatever the mode mixity provided both T-stress magnitude and shear to opening critical ERR ratio are sufficiently small (Fig. 16i, a, b, d, e). On one hand, increasing the T-stress magnitude decreases facet nucleation apparent SIF while not influencing straight crack propagation apparent SIF (see for instance Fig. 16a, d, g). Therefore, facet nucleation becomes more likely for sufficiently large T-stress magnitudes for mode mixities up to a certain value that increases with increasing T-stress magnitude. On the other hand, increasing $\mathcal{G}_{\mathrm{IIIc}}/\mathcal{G}_{\mathrm{Ic}}$ increases the straight crack propagation apparent SIF while not influencing much facet nucleation apparent SIF (see for instance Fig. 16d, e, f). Therefore, facet nucleation becomes more likely for sufficiently large $\mathcal{G}_{\mathrm{IIIc}}/\mathcal{G}_{\mathrm{Ic}}$ especially for mode mixities larger than a certain value that decreases with increasing $\mathcal{G}_{\mathrm{IIIc}}/\mathcal{G}_{\mathrm{Ic}}$.

Configurations for which facet nucleation is more favorable than straight crack propagation are finally summarized in Fig. 17.

Increasing $\mathcal{G}_{\mathrm{IIIc}}/\mathcal{G}_{\mathrm{Ic}}$ ratio mainly tends to increase straight crack propagation SIF, this increase being more pronounced for larger mode mixities. As a consequence, it tends to make facet nucleation more favorable than straight crack propagation for mode mixities larger than a given value depending on $\mathcal{G}_{\mathrm{IIIc}}/\mathcal{G}_{\mathrm{Ic}}$. The determination of the configurations for which facet nucleaction is more favorable than straight crack propagation indicates that this phenomenon does not depend on a threshold in terms of $K_{\mathrm{III}}/K_{\mathrm{I}}$ for $\mathcal{G}_{\mathrm{IIIc}}/\mathcal{G}_{\mathrm{Ic}} < 10$ (Fig. 17a, b) or normalized T-stress magnitude $T_3/\sigma_c > 0.075$ (Fig. 17c, d). It means that facet nucleation actually depends on the material through the ratio between shear and opening critical ERR and on the loading, not only in terms of mode mixity but also in terms of T-stress magnitude. The influence of the Poisson's ratio is finally shown on Fig. 17d, a similar influence of the Poisson's ratio being obtained for other $\mathcal{G}_{\mathrm{IIIc}}/\mathcal{G}_{\mathrm{Ic}}$ ratios. The same reasoning as previously is followed except that ν varies, which results in a variation in the dimensionless IERR (see functions given in the Appendix for several Poisson's ratio) and stress fields. The Poisson's

ratio has an influence on the boundary of the domain corresponding to facet nucleation being more favorable than straight crack propagation. For β smaller than ≈ 0.6, increasing the Poisson's ratio results in a decrease in the required T-stress magnitude for facet initiation. For T/σ_c smaller than 0.05, increasing the Poisson's ratio results in increasing the minimum mode mixity for which facet nucleation occurs.

7 Conclusion

Considering that crack segmentation in mode I+III results from the nucleation and then propagation of facets, it is essential to explain why the apparition of facets is favored energetically in comparison to straight propagation. Using the CC, we show that:

(i) In absence of T-stress and mode dependent fracture toughness $\mathcal{G}_{\mathrm{IIIc}}/\mathcal{G}_{\mathrm{Ic}}$, straight propagation should occur whatever the mode mixity $K_{\mathrm{III}}/K_{\mathrm{I}}$;
(ii) It is necessary to take into account jointly the contribution of T-stress and mode dependent fracture properties to be in line with experimental observations.

More precise outputs of the CC are that facet nucleation:

(i) Cannot occur for too small T-stress magnitude and $\mathcal{G}_{\mathrm{IIIc}}/\mathcal{G}_{\mathrm{Ic}}$ levels;
(ii) Becomes more favorable than straight crack propagation either for sufficiently large T-stress magnitude and small mode mixities or for sufficiently large $\mathcal{G}_{\mathrm{IIIc}}/\mathcal{G}_{\mathrm{Ic}}$ and large mode mixities.

The physical ingredients behind these results are twofold. First, increasing the T-stress magnitude decreases the load needed for facet nucleation that makes them more keen to appear. Second, a significant amount of shear critical energy release rate $\mathcal{G}_{\mathrm{IIIc}}$ increases the load required for straight crack propagation especially for sufficiently large mode mixities, tending to disadvantage straight propagation. A perspective of this work will be to design specific experiments to evaluate these results, as well as evidencing the proposed theory and its possible limitations based on existing experiments in the literature. For instance, the complex wedge and compressive loading proposed in Pham and Ravi-Chandar (2016) is expected to induce a local combined mode I+III and T-stress ahead of the primary crack. Nevertheless, in other works, facet nucleation is also observed under almost pure mode I configurations (Lin et al. 2010; Ronsin et al. 2014), in which the T-stress level might be negligible. In such configurations, it will be necessary to evaluate if the proposed scenario is sufficient to explain facet nucleation.

Author contributions AD performed numerical simulations and drafted the manuscript. Dl helped with the matched asymptotic approach of the coupled criterion All authors developed the methodology, conceived of the study, and participated in its design, coordination, and critical review of the manuscript. All authors read and approved the final manuscript.

Declarations

Competing interests The authors declare no competing interests.

Appendix

The functions A_{ij}, B_i, C are given in Fig. 18 as a function of φ in complement of Fig. 3 for different Poisson's ratio between $\nu = 0$ and $\nu = 0.48$.

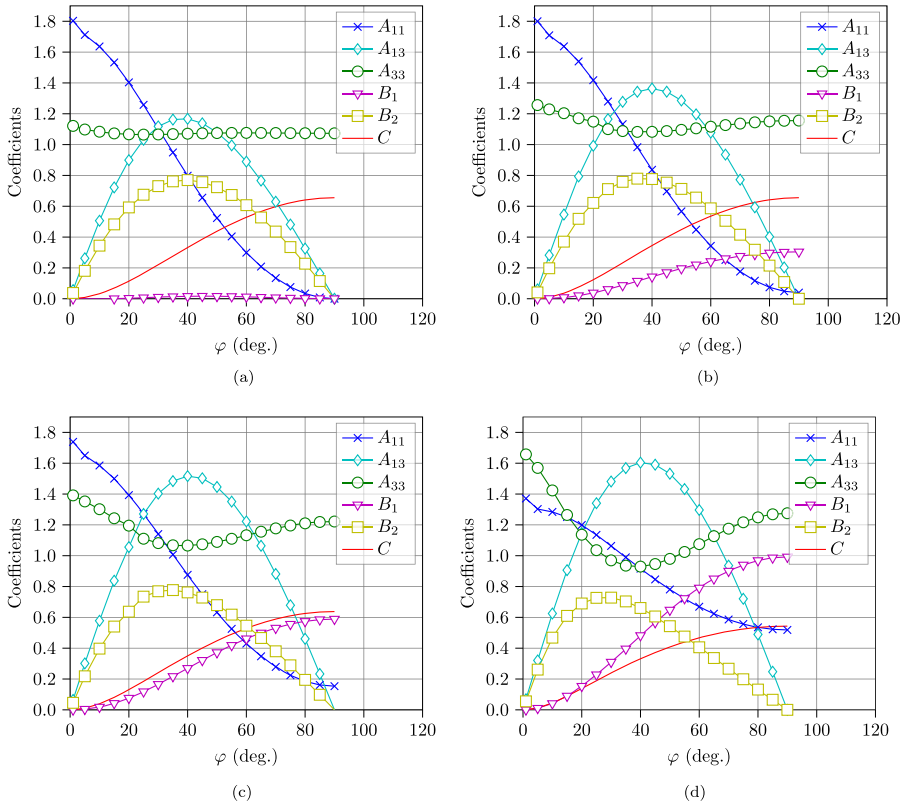

Fig. 18 Variation of the normalized IERR coefficients as a function of the crack orientation obtained for **a** $\nu = 0$, **b** $\nu = 0.12$, **c** $\nu = 0.24$ and **d** $\nu = 0.48$

References

Amestoy M, Leblond J (1992) Crack paths in plane situations—II. Detailed form of the expansion of the stress intensity factors. Int J Solids Struct 29:465–501. https://doi.org/10.1016/0020-7683(92)90210-K

Buchholz F, Chergui A, Richard H (2004) Fracture analyses and experimental results of crack growth under general mixed mode loading conditions. Eng Fract Mech 71(4):455–468. https://doi.org/10.1016/S0013-7944(03)00015-8

Cambonie T, Lazarus V (2014) Quantification of the crack fragmentation resulting from mode I + III loading. Procedia Mater Sci 3:1816–1821. https://doi.org/10.1016/j.mspro.2014.06.293

Chen C, Cambonie T, Lazarus V, Nicoli M, Pons A, Karma A (2015) Crack front segmentation and facet coarsening in mixed-mode fracture. Phys Rev Lett 115:265503. https://doi.org/10.1103/PhysRevLett.115.265503

Citarella R, Buchholz F (2008) Comparison of crack growth simulation by DBEM and fem for SEN-specimens undergoing torsion or bending loading. Eng Fract Mech 75(3):489–509. https://doi.org/10.1016/j.engfracmech.2007.03.039

Cox S, Scholz C (1988) On the formation and growth of faults: an experimental study. J Struct Geol 10(4):413–430. https://doi.org/10.1016/0191-8141(88)90019-3

Davenport J, Smith D (1993) A study of superimposed fracture modes I, II and III on PMMA. Fatigue Fract Eng Mater Struct 16(10):1125–1133. https://doi.org/10.1111/j.1460-2695.1993.tb00082.x

Dhondt G, Chergui A, Buchholz F (2001) Computational fracture analysis of different specimens regarding 3D and mode coupling effects. Eng Fract Mech 68(4):383–401. https://doi.org/10.1016/S0013-7944(00)00104-1

Doitrand A, Leguillon D (2018) Numerical modeling of the nucleation of facets ahead of a primary crack under mode I + III. Int J Fract 123(1):37–50. https://doi.org/10.1007/s10704-018-0305-8

Doitrand A, Leguillon D (2021) Asymptotic analysis of pore crack initiation near a free edge. Theor Appl Fract Mech 116:103125. https://doi.org/10.1016/j.tafmec.2021.103125

Doitrand A, Leguillon D, Martin E (2020a) Computation of generalized stress intensity factors of 3D singularities. Int J Solids Struct 190:271–280. https://doi.org/10.1016/j.ijsolstr.2019.11.019

Doitrand A, Martin E, Leguillon D (2020b) Numerical implementation of the coupled criterion: matched asymptotic and full finite element approaches. Finite Elem Anal Des 168:103344. https://doi.org/10.1016/j.finel.2019.103344

Eberlein A, Richard H, Kullmer G (2017) Facet formation at the crack front under combined crack opening and anti-plane shear loading. Eng Fract Mech 174:21–29. https://doi.org/10.1016/j.engfracmech.2016.12.004

Erdogan G, Sih G (1963) On the crack extension in plates under plane loading and transverse shear. ASME J Basic Eng 85:519–527. https://doi.org/10.1115/1.3656897

Francfort G, Marigo J (1998) Revisiting brittle fracture as an energy minimization problem. J Mech Phys Solids 46:1319–1342. https://doi.org/10.1016/S0022-5096(98)00034-9

Goldstein R, Osipenko N (2012) Successive development of the structure of a fracture near the front of a longitudinal shear crack. Dokl Phys 57:281–284. https://doi.org/10.1134/S1028335812070087

Goldstein R, Salganik R (1974) Brittle fracture of solids with arbitrary cracks. Int J Fract 10:507–523. https://doi.org/10.1007/BF00155254

Gravouil A, Moes N, Belytschko T (2002) Non-planar 3D crack growth by the extended finite element and level sets-part II: level set update. Int J Numer Methods Eng 53:2569–2586. https://doi.org/10.1002/nme.430

Hattali M, Cambonie T, Lazarus V (2021) Toughening induced by the formation of facets in mode I + III brittle fracture: experiments versus a two-scale cohesive zone model. J Mech Phys Solids 156:104596. https://doi.org/10.1016/j.jmps.2021.104596

Henry H (2016) Crack front instabilities under mixed mode loading in three dimensions. EPL 114(6):66001

Hull D (1994) The effect of mixed mode I/III on crack evolution in brittle solids. Int J Fract 70:59–79. https://doi.org/10.1007/BF00018136

Hutchinson J, Suo Z (1992) Mixed mode cracking in layered materials. Adv Appl Mech. https://doi.org/10.1016/S0065-2156(08)70164-9

Knauss W (1970) An observation of crack propagation in anti-plane shear. Int J Fract 6:183–187. https://doi.org/10.1007/BF00189825

Lazarus V, Leblond J, Mouchrif S (2001) Crack front rotation and segmentation in mixed mode I + III or I + II + III. Part II: comparison with experiments. J Mech Phys Solids 49(7):1421–1443. https://doi.org/10.1016/S0022-5096(01)00008-4

Lazarus V, Buchholz F, Fulland M, Wiebesiek J (2008) Comparison of predictions by mode II or mode III criteria on crack front twisting in three or four point bending experiments. Int J Fract 153:141–151. https://doi.org/10.1007/s10704-008-9307-2

Lazarus V, Prabel B, Cambonie T, Leblond J (2020) Mode I + III multiscale cohesive zone model with facet coarsening and overlap: solutions and applications to facet orientation and toughening. J Mech Phys Solids 141:104007. https://doi.org/10.1016/j.jmps.2020.104007

Lebihain M, Leblond J, Ponson L (2022) Crack front instability in mixed-mode I + III: the influence of non-singular stresses. Eur J Mech A. https://doi.org/10.1016/j.euromechsol.2022.104602

Leblond J, Karma A, Lazarus V (2011) Theoretical analysis of crack front instability in mode I + III. J Mech Phys Solids 59(9):1872–1887. https://doi.org/10.1016/j.jmps.2011.05.011

Leblond J, Lazarus V, Karma A (2015) Multiscale cohesive zone model for propagation of segmented crack fronts in mode I + III fracture. Int J Fract 191:167–189. https://doi.org/10.1007/s10704-015-0001-x

Leblond J, Karma A, Ponson L, Vasudevan A (2019) Configurational stability of a crack propagating in a material with mode-dependent fracture energy—part I: mixed-mode I + III. J Mech Phys Solids 126:187–203. https://doi.org/10.1016/j.jmps.2019.02.007

Leguillon D (2002) Strength or toughness? A criterion for crack onset at a notch. Eur J Mech A 21(1):61–72. https://doi.org/10.1016/S0997-7538(01)01184-6

Leguillon D, Murer S (2008) Crack deflection in a biaxial stress state. Int J Fract 150:75. https://doi.org/10.1007/s10704-008-9231-5

Leguillon D, Sanchez-Palencia E (1987) Computation of singular solutions in elliptic problems and elasticity. Wiley, Hoboken

Leguillon D, Yosibash Z (2017) Failure initiation at V-notch tips in quasi-brittle materials. Int J Solids Struct 122–123:1–13. https://doi.org/10.1016/j.ijsolstr.2017.05.036

Lin B, Mear M, Ravi-Chandar K (2010) Criterion for initiation of cracks under mixed-mode I + III loading. Int J Fract 165:175–188. https://doi.org/10.1007/s10704-010-9476-7

Liu S, Chao Y, Zhu X (2004) Tensile-shear transition in mixed mode I/III fracture. Int J Solids Struct 41(22–23):6147–6172. https://doi.org/10.1016/j.ijsolstr.2004.04.044

Mittelman B, Yosibash Z (2015) Energy release rate cannot predict crack initiation orientation in domains with a sharp V-notch under mode III loading. Eng Fract Mech 141:230–241. https://doi.org/10.1016/j.engfracmech.2015.05.008

Molnár G, Doitrand A, Jaccon A, Prabel B, Gravouil A (2022) Thermodynamically consistent linear-gradient damage model in Abaqus. Eng Fract Mech 266:108390. https://doi.org/10.1016/j.engfracmech.2022.108390

Palaniswamy K, Knauss W (1978) On the problem of crack extension in brittle solids under general loading. In: Nemat-Nasser S (ed) Mechanics today. Pergamon, pp 87–148. https://doi.org/10.1016/B978-0-08-021792-5.50010-0

Pandolfi A, Ortiz M (2012) An eigenerosion approach to brittle fracture. Int J Numer Methods Eng 92(8):694–714. https://doi.org/10.1002/nme.4352

Pham K, Ravi-Chandar K (2014) Further examination of the criterion for crack initiation under mixed mode I + III loading. Int J Fract 189:121–138. https://doi.org/10.1007/s10704-014-9966-0

Pham K, Ravi-Chandar K (2016) On the growth of cracks under mixed-mode I + III loading. Int J Fract 199:105–134. https://doi.org/10.1007/s10704-016-0098-6

Pham K, Ravi-Chandar K (2017) The formation and growth of echelon cracks in brittle materials. Int J Fract 206:229–244. https://doi.org/10.1007/s10704-017-0212-4

Pham K, Ravi-Chandar K, Landis C (2017) Experimental validation of a phase-field model for fracture. Int J Fract 205(1):83–101. https://doi.org/10.1007/s10704-017-0185-3

Pollard D, Segall P, Delaney P (1982) Formation and interpretation of dilatant echelon cracks. GSA Bull 93(12):1291–1303. https://doi.org/10.1130/0016-7606(1982)93<1291:FAIODE>2.0.CO;2

Pons A, Karma A (2010) Helical crack-front instability in mixed-mode fracture. Nature 464:85–89. https://doi.org/10.1038/nature08862

Ronsin O, Caroli C, Baumberger T (2014) Crack front échelon instability in mixed mode fracture of a strongly non-

linear elastic solid. EPL 105(3):34001. https://doi.org/10.1209/0295-5075/105/34001

Sommer E (1969) Formation of fracture 'lances' in glass. Eng Fract Mech 1:539–546. https://doi.org/10.1016/0013-7944(69)90010-1

Vojtek T, Pippan R, Hohenwarter A, Holáň L, Pokluda J (2013) Near-threshold propagation of mode II and mode III fatigue cracks in ferrite and austenite. Acta Mater 61(12):4625–4635. https://doi.org/10.1016/j.actamat.2013.04.033

Vojtek T, Hohenwarter A, Pippan R, Pokluda J (2016) Experimental evidence of a common local mode II growth mechanism of fatigue cracks loaded in modes II, III and II+ III in niobium and titanium. Int J Fatigue 92:470–477. https://doi.org/10.1016/j.ijfatigue.2016.02.042

Yosibash Z, Mittelman B (2016) A 3D failure initiation criterion from a sharp V-notch edge in elastic brittle structures. Eur J Mech A 60:70–94. https://doi.org/10.1016/j.euromechsol.2016.06.003

Younes A, Engelder T (1999) Fringe cracks: key structures for the interpretation of the progressive Alleghanian deformation of the Appalachian plateau. Bull Geol Soc Am 111(2):219–239. https://doi.org/10.1130/0016-7606(1999)111<0219:FCKSFT>2.3.CO;2